

# The environments and ages of extragalactic radio sources inferred from multi-frequency radio maps

C. R. Kaiser

Max-Planck-Institut für Astrophysik, Postfach 1317, Karl-Schwarzschild-Str.1, D-85741 Garching, GERMANY

Received 1.5.2000 / Accepted <date>

**Abstract.** A 3-dimensional model of the synchrotron emissivity of the cocoons of powerful extragalactic radio sources of type FR II is constructed. Bulk backflow and energy losses of the relativistic electrons, radiative and adiabatic, are self-consistently taken into account. Thus the model is an extension of spectral aging methods including the underlying source dynamics into the age estimates. The discrepancies between spectral ages and dynamical ages arising from earlier methods are resolved. It is also shown that diffusion of relativistic particles within the cocoon is unlikely to significantly change the particle spectrum and thus the emitted radio spectrum. Projection along the line of sight yields 1 or 2-dimensional surface brightness distributions which can be compared with observations. From the model parameters constraints on the source age, the density of the source environment and the angle to the line of sight can be derived. Application of the method to Cygnus A, 3C 219 and 3C 215 show that the method provides robust estimates for the model parameters for sources with comparatively regularly shaped radio lobes. The resolution of the radio maps required is only moderate. Within the large uncertainties for the orientation angle, the three example sources are found to be consistent with orientation-based unification schemes of radio-loud AGN. In the case of Cygnus A the gas density of the environment is found to agree with independent X-ray measurements. For 3C 219 and 3C 215 the densities derived from the model are apparently too low. It is suggested that these discrepancies are caused by overestimates of slope and core radius of  $\beta$ -models for the gas density distribution from X-ray observations for clusters hosting powerful radio sources.

**Key words:** Galaxies: active – Galaxies: individual: Cygnus A – Galaxies: individual: 3C 219 – Galaxies: jets – Quasars: individual: 3C 215 – Radio continuum: galaxies

## 1. Introduction

The ‘standard model’ of extragalactic classical double radio sources by Scheuer (1974) explains these sources as twin jets emerging from the Active Galactic Nucleus (AGN) and impinging on the surrounding gas. The compact, high surface brightness regions or hot spots at the end of the jets are interpreted as the sites of the interaction between the jets and the environment. After passing through the hot spot region, the jet material inflates the radio lobes or cocoon which is observed as diffuse emission in between the hot spots and the source core (e.g. Muxlow & Garrington 1991 and references therein). This picture forms the basis of virtually all more recent attempts at modeling the dynamics and radio emission properties of powerful radio galaxies and radio-loud quasars (Begelman & Cioffi 1989, Falle 1991, Daly 1994, Nath 1995, Kaiser & Alexander 1997, Chyży 1997, Kaiser et al. 1997, Blundell et al. 1999).

These models for the evolution of individual classical doubles or FR II-type objects (Fanaroff & Riley 1974) can be used to study the cosmological evolution of the population as a whole. One of the more important trends is the apparent decrease of the mean linear size of the radio structures with increasing redshift (see Neeser et al. 1995 and references therein).

Two recent attempts in fully explaining the linear size – redshift anti-correlation were presented by Blundell et al. (1999) and Kaiser & Alexander (1999a). Blundell et al. argue that a specific form of pre-aging of the relativistic particle population in the hot spots in connection with the lower flux limit of complete observed samples causes this anti-correlation (the so-called youth-redshift degeneracy, Blundell et al. 1999, Blundell & Rawlings 1999). Alternatively, Kaiser & Alexander propose that the apparent smaller sizes of radio sources at high redshift could be caused by a denser environment of these objects at high redshift. Clearly, the evolution or non-evolution of the radio source environments is of great interest to decide this and other important cosmological questions.

Various methods have been employed in determining the properties of the radio source environments. X-ray ob-

servations of the hot gas around radio sources in clusters yield direct estimates of the gas density (Crawford et al. 1999, Hardcastle & Worrall 1999). However, such studies are at present confined to objects at low redshifts. Furthermore, the AGN (e.g. Sambruna et al. 1999) and the large-scale radio structure contribute to the X-ray emission (Brunetti et al. 1999, Kaiser & Alexander 1999b, Sect. 6). The properties of the density distribution inferred from X-ray observations may therefore be considerably influenced by the presence of the radio source itself.

Faraday rotation of the polarisation angle of the synchrotron emission and the related depolarisation can be used to determine the gas density of the material surrounding the radio lobes (e.g. Garrington et al. 1988, Laing 1988). Unfortunately, this method does not provide a direct measure of the gas density as the rotation measure also depends on the strength of the magnetic field in the source environment. Usually it is not possible to break this degeneracy because the strength of the magnetic field is only poorly known.

Constraints on the density of the radio source environments also come from optical or infrared galaxy counts around the host galaxies (e.g. Hill & Lilly 1991). It is not straightforward to decide whether galaxies in the field of the radio source host are associated or chance background objects. Resolving the ambiguity would ideally require the spectroscopic measurement of the redshifts of all objects in question. This is very time consuming. In any case, the method provides only indirect constraints on the gas density around the radio source as this has to be inferred from comparison with low redshift clusters or groups of similar richness.

The ages of powerful radio sources can in principle be determined from their radio spectrum (e.g. Alexander & Leahy 1987). The various energy losses of the relativistic particles depend on time and so the shape of the radio spectrum contains an encoded history of the source. In practice the time-dependence of the energy losses complicates the estimation of the spectral age because different parts of the source have different ages. Even when radio maps at various frequencies which fully resolve the radio lobes are used, it is difficult to disentangle the effects of the various loss mechanisms and possible bulk backflow of the cocoon material along the jet (e.g. Rudnick et al. 1994).

The model developed in this paper aims at tracing the individual evolution of parts of the cocoon and thereby providing more accurate estimates for the source age. At the same time the model also constrains the density in the source environment and other parameters like the energy transport rate of the jets. It is solely based on radio observations which are available for a large number of objects, even at high redshift. This model may therefore provide an important step in determining the cosmological evolution of the FR II radio source population.

In Sect. 2 I show that diffusion of relativistic particles in the cocoons of FR II-type objects should not significantly change the energy distribution of particles. In Sect. 3 the dynamical model of Kaiser & Alexander (1997, hereafter KA) and its extension by Kaiser et al. (1997, hereafter KDA) to include synchrotron emission are briefly summarised. A 3-dimensional model of the synchrotron emissivity of the cocoon based on this analysis is constructed in Sects. 3.3 and 3.4. Methods for comparing the model predictions with observations are developed in Sect. 4. The degeneracy of model parameters resulting from the comparison method is also discussed here. The model is then applied to three FR II-type radio sources, Cygnus A, 3C 219 and 3C 215, in Sect. 5. The results are discussed in Sect. 6. The main conclusions are summarised in Sect. 7.

Throughout this paper I use  $H_0 = 50 \text{ km s}^{-1} \text{ Mpc}^{-1}$  and  $q_0 = 0$ .

## 2. Comparison to spectral aging methods

The age of extragalactic radio sources can be estimated by the use of spectral aging arguments. This method relies on the determination of the break in the radio spectrum caused by the time-dependent energy losses of the relativistic electrons within the cocoon (e.g. Alexander & Leahy 1987). At frequencies higher than the break frequency,  $\nu_b$ , the spectrum significantly steepens due to the radiative energy losses of the electrons. The spectral age of a electron population,  $t_{sa}$ , with observed break frequency  $\nu_b$  within a magnetic field of strength  $B$  which does not vary in time is proportional to  $B^{-3/2} \nu_b^{-1/2}$ . Despite the implication of source dynamics that the magnetic field does vary in time, the constant field relation is usually used in determining the spectral age of a given source. In general the strength of the magnetic field will decrease while the source expands and so  $t_{sa}$  will be an overestimate of the true source age,  $t$ . However, because of variations of the magnetic field in the cocoon and the backflow of gas in this region,  $t_{sa}$  is usually found to be lower than the dynamical ages inferred from the advance speed of the cocoon by various methods (Alexander & Leahy 1987).

The model presented in the following can be viewed as an extension of the spectral aging formalism. Within the cocoon it traces the evolution of the local magnetic field in time. This allows the accurate determination of the energy distribution function of the relativistic particle population and thus the emitted spectrum at a given location along the cocoon. It is therefore not surprising that the model predicts an older age for Cygnus A (see Sect. 4) than the classical spectral index analysis of Carilli et al. (1991). The combination of a dynamical model with the accurate treatment of the local evolution within the cocoon of the radio emission properties implies that the spectral and dynamical ages are identical.

### 2.1. Diffusion of relativistic particles

In the context of spectral aging methods other processes changing the energy distribution of the relativistic electrons and thus invalidating the age estimates have been put forward. These are summarised and discussed by Blundell & Rawlings (2000). They show that most of these processes are rather inefficient and will not strongly influence spectral aging methods or the model discussed here. However, Blundell & Rawlings (2000) claim that the anomalous diffusion mechanism of Rechester & Rosenbluth (1978) can lead to very fast diffusion of relativistic particles through the tangled magnetic field in the cocoon. So much so that the radio spectra observed at any point along the cocoon essentially arise from the electrons accelerated by the jet shock at the hot spot within the last  $10^6$  years of the observation. This would imply that no information on the source age can be derived from the spatial properties of the observed emission. Support for a universal particle energy spectrum may come from the interpretation of observations of Cygnus A by Katz-Stone et al. (1993), Rudnick et al. (1994) and Katz-Stone & Rudnick (1994). They find that a single, non-power law spectrum shifted in frequency by the local strength of the magnetic field is emitted by all parts of the lobes of Cygnus A. Note however, that the spectral shape they find may be caused by the free-free absorption in our own galaxy of the emission of Cygnus A at low frequencies (Carilli et al. 1991). In this case, the universal spectrum is simply explained by shifting an aging energy spectrum of relativistic particles which is not a single power law. Alternatively, changes in the strength of the magnetic field along a given line of sight may also introduce additional curvature in the observed spectrum (Rudnick et al. 1994). The mentioned interpretation of the radio observations of Cygnus A in itself is therefore no proof of efficient diffusion acting in the lobes of radio galaxies.

In the appendix I show that anomalous diffusion is probably much less effective in the cocoon plasma as previously thought. In general we do not observe any signature for diffusion losses of the cocoons of radio sources and so diffusion will not alter the distribution of relativistic particles within the cocoon. This allows us to use the spatial distribution of the synchrotron radio emission of FR II sources to infer their age. The model developed in the following can be viewed as an extension to the classical spectral aging methods in that it takes into account the evolution of the magnetic field in the lobe.

### 3. The model

In this Sect. I briefly summarise the dynamical and radiative model that form the basis for the extended treatment presented in this paper. Following this the prescription for the spatial distribution of the synchrotron emission within the radio lobes is developed.

### 3.1. The dynamical model

The large scale structure of radio galaxies and radio-loud quasars of type FR II is formed by twin jets emanating from the central AGN buried inside the nucleus of the host galaxy. The jets propagate into opposite directions from the core of the source. They end in strong jet shocks and, after passing through these shock, the jet material inflates the cocoon surrounding the jets. The cocoon is overpressured with respect to the ambient medium and therefore drives strong bow shocks into this material.

Falle (1991) and KA showed that the expansion of the bow shock and the cocoon should be self-similar which is supported by observations (e.g. Leahy & Williams 1984, Leahy et al. 1989, Black 1992). In these models the density distribution of the material the radio source is expanding into is approximated by a power law,  $\rho_x = \rho_o(r/a_o)^{-\beta}$ , where  $r$  is the radial distance from the source centre and  $a_o$  is the core radius of the density distribution. X-ray observations of groups and clusters of galaxies show that the density of the hot gas in these structures is often distributed according to (e.g. Sarazin 1988)

$$\rho_x = \frac{\rho_o}{\left[1 + (r/a_o)^2\right]^{3\beta'/2}}. \quad (1)$$

Outside a few core radii,  $a_o$ , the power law assumed above with  $\beta = 3\beta'$  provides an adequate fit to Eq. (1). Even for smaller distances  $r$  good power law approximations can be found by adjusting  $\beta$  and  $\rho_o$  (e.g. Kaiser & Alexander 1999a).

In the model of KA it is also assumed that the rate at which energy is transported along each jet,  $Q_o$ , is constant and that the jets are in pressure equilibrium with their own cocoon. The very high sound speed within the cocoon results in a practically uniform pressure within this region apart from the tip of the cocoon. The pressure in this ‘hot spot’ region, named for the very strong radio emission originating in the shock at the end of the jets, is somewhat higher as the cocoon material injected by the jets at these points is not yet in pressure equilibrium with the rest of the cocoon.

In the following I will concentrate on only one jet and the half of the cocoon it is contained in. From KA I take the expressions for the evolution of the uniform cocoon pressure,

$$p_c = \frac{18c_1^{2(5-\beta)/3}}{(\Gamma_x + 1)(5 - \beta)^2 P_{hc}} (\rho_o a_o^\beta Q_o^2)^{1/3} L_j^{(-4-\beta)/3}, \quad (2)$$

and that of the physical length of the jet,

$$L_j = c_1 \left(\frac{Q_o}{\rho_o a_o^\beta}\right)^{1/(5-\beta)} t^{3/(5-\beta)}. \quad (3)$$

Here,  $\Gamma_x$  is the ratio of specific heats of the gas surrounding the radio source,  $t$  is the age of the jet flow and  $c_1$  is a

dimensionless constant. The ratio,  $P_{\text{hc}}$ , of the pressure in the hot spot region and  $p_c$  is constant in the model of KA.

KDA extend the model of KA to include the synchrotron emission of the cocoon. This is done by splitting up the cocoon into small volume elements,  $\delta V_c$ , the evolution of which is then followed individually. By assuming that these elements are injected by the jet into the hot spot region at time  $t_i$  during a short time interval  $\delta t_i$  and then become part of the cocoon, KDA find

$$\delta V_c = \frac{(\Gamma_c - 1) Q_o}{p_c(t_i)} (P_{\text{hc}})^{(1-\Gamma_c)/\Gamma_c} \left(\frac{t}{t_i}\right)^{c_4} \delta t_i, \quad (4)$$

where  $\Gamma_c$  is the ratio of specific heats for the cocoon material and  $c_4 = (4 + \beta) / [\Gamma_c (5 - \beta)]$ . Because the expansion of the cocoon is self-similar we can set for the volume of the total volume of the cocoon, following the notation of KA,  $V_c = c_3 L_j^3$ , where  $c_3$  is a dimensionless constant and depends on the geometric shape of the cocoon. In order to ensure self-consistency the integration of Eq. (4) over the injection time from  $t_i = 0$  to  $t_i = t$  must be equal to the total cocoon volume  $V_c$ . Substituting Eq. (3) for  $L_j$  then yields

$$c_1 = \left[ P_{\text{hc}}^{1/\Gamma_c} \frac{\Gamma_c (\Gamma_c - 1) (\Gamma_x + 1) (5 - \beta)^3}{18c_3 (9\Gamma_c - 4 - \beta)} \right]^{1/(5-\beta)}. \quad (5)$$

Note, that this expression for  $c_1$  is different from the one given by KA. In their analysis they used the expression for conservation of energy for the entire cocoon

$$dU_c = \frac{1}{\Gamma_c - 1} [d(p_c V_c) + d(p_h V_h)] = Q_o dt, \quad (6)$$

where  $V_h$  is the volume of the hot spot region with pressure  $p_h$ . KA then used the simplifying assumption that the cocoon has a cylindrical geometry, the expansion of which is governed along the jet axis by  $p_h$  while its growth perpendicular to this direction is driven by  $p_c$ . This implies  $p_h/p_c = P_{\text{hc}} = 4R_T^2$ , where  $R_T$  is the ratio of the length of one jet and the full width of the associated lobe halfway down the jet. Kaiser & Alexander (1999b) subsequently derived empirical fitting formulae for  $P_{\text{hc}}$  as functions of  $\beta$  and  $R_T$  from an analysis of the flow of shocked gas between the bow shock and the cocoon. Their results showed that the original approximation tends to overestimate the value of  $P_{\text{hc}}$ . In the following I use a generalised empirical fitting formula based on their result and further calculations with additional values of  $\beta$ ,

$$P_{\text{hc}} = (2.14 - 0.52\beta) R_T^{2.04 - 0.25\beta}. \quad (7)$$

In order to satisfy Eqs. (5) and (6) I now generalise the approach of KA by setting  $d(p_h V_h) = f d(p_c V_c)$ . Because of the self-similar expansion of the cocoon  $f$  is a constant and will depend on the ratio  $P_{\text{hc}}$ . The strict separation of the cocoon material into the hot spot region and the rest of the cocoon with two distinctly different values of the

respective pressure within these regions is of course artificial. In the cocoons of real FR II objects the transition of jet material from hot spot to cocoon will be accomplished in a continuous hydrodynamical flow along a pressure gradient much smoother than the sudden change from  $p_h$  to  $p_c$  described here. However, a detailed model of this flow is beyond the scope of this paper and for simplicity I will use the assumption of a strict spatial separation in the following. As the two cocoon regions are in physical contact with each other,  $f$  may become negative as the expansion of one region may influence the evolution of the other. Substituting Eqs. (2) and (3) into Eq. (6) gives

$$f = \frac{P_{\text{hc}}^{(\Gamma_c - 1)/\Gamma_c} - \Gamma_c}{\Gamma_c P_{\text{hc}}}.$$

### 3.2. Synchrotron emission

The cocoon volume elements  $\delta V_c$  are filled with a magnetised plasma and a population of relativistic electrons accelerated at the shock terminating the jet flow at the hot spot. They therefore emit synchrotron radio radiation. In optically thin conditions the monochromatic luminosity due to this process can be calculated by folding the emissivity of single electrons with their energy distribution (e.g. Shu 1991).

Following KDA I assume that the initial energy distribution of the relativistic electrons as they leave the acceleration region of the hot spot follows a power law with exponent  $-p$  between  $\gamma = 1$  and  $\gamma = \gamma_{\text{max}}$ . The electrons are subject to energy losses due to the adiabatic expansion of  $\delta V_c$ , the emission of synchrotron radiation and inverse Compton scattering of the CMB. For a given volume element at time  $t$  that was injected into the cocoon at time  $t_i$  these losses result in an energy distribution (see KDA)

$$n'(x) = n_o(t_i) \left(\frac{2\nu}{3\nu_L x}\right)^{-p/2} \left(\frac{t_i}{t}\right)^{c_4(p+2)/3} \times \left(1 - c_5 \sqrt{\frac{2\nu}{3\nu_L x}}\right)^{p-2}, \quad (8)$$

with

$$c_5 = \frac{4\sigma_T}{3m_e c} t \times \left\{ \frac{u_B}{c_6} \left[1 - \left(\frac{t_i}{t}\right)^{c_6}\right] + \frac{u_{\text{cmb}}(z)}{c_7} \left[1 - \left(\frac{t_i}{t}\right)^{c_7}\right] \right\}, \quad (9)$$

where  $u_{\text{cmb}}(z)$  is the energy density of the CMB radiation field at the source redshift  $z$  and  $m_e$  is the rest mass of an electron. Here I have used  $c_6 = 1 - c_4 (\Gamma_B + 1/3)$  and  $c_7 = 1 - c_4/3$ . The normalisation of the energy spectrum,  $n_o(t_i)$ , is given by integrating the initial power law distribution over the entire energy range

$$n_o(t_i) = \frac{u_e(t_i)}{m_e c^2} \times \left[ \frac{1}{2-p} (\gamma_{\text{max}}^{2-p} - 1) - \frac{1}{1-p} (\gamma_{\text{max}}^{1-p} - 1) \right]^{-1}, \quad (10)$$

or, for  $p = 2$ ,

$$n_o(t_i) = \frac{u_e(t_i)}{m_e c^2} \left[ \log(\gamma_{\max}) + \left( \frac{1}{\gamma_{\max}} - 1 \right) \right]^{-1}, \quad (11)$$

where  $u_e$  is the total energy density of the relativistic particle distribution. At time  $t_i$  I set  $u_B(t_i)/u_e(t_i) = r$  and for simplicity  $p_c(t_i) = (\Gamma_c - 1)[u_B(t_i) + u_e(t_i)]$ . In the following I assume that the minimum energy condition (e.g. Miley 1980) is initially fulfilled in each volume element  $\delta V_c$  and therefore  $r = (p + 1)/4$ . From Eqs. (2) and (3) it follows that  $p_c(t_i) = p_c(t)(t/t_i)^{c_4 \Gamma_c}$  and with the assumption of completely tangled magnetic fields I find  $u_B(t) = u_B(t_i)(t/t_i)^{c_4 \Gamma_B}$  (see also KA). With this the set of equations describing the radio synchrotron emissivity,  $\epsilon_\nu = P_\nu/\delta V_c$ , of a given volume element injected into the cocoon at time  $t_i$  only depends on the present value of the pressure in the cocoon,  $p_c(t)$ , and the age of the radio source,  $t$ .

### 3.3. Spatial distribution of the emission

So far the cocoon volume elements  $\delta V_c$  were only characterised by their injection time into the cocoon,  $t_i$ . From the analysis above it is not possible to decide where they are located spatially in the cocoon.

From the above analysis it is clear that the radio spectrum emitted by a given cocoon volume element depends on the ‘energy loss history’ of this part of the cocoon. Adiabatic losses only change the normalisation of the emitted spectrum while its slope at a given frequency is governed by the radiative loss processes of the relativistic electrons. In the model described above the strength of the magnetic field which determines the magnitude of synchrotron losses is tied to the pressure in the cocoon,  $p_c$ . The value of  $p_c$  in turn depends on the energy transport rate of the jet,  $Q_o$ , and a combination of parameters describing the density distribution of the gas the cocoon is expanding into,  $\rho_o a_o^\beta$ . In the analytical scenario presented here the volume elements are the building blocks of the cocoon and the variation of the radio surface brightness of the cocoon of an FR II along its major axis can therefore potentially provide information on the properties of the source environment. For this I now identify the cocoon volume elements  $\delta V_c$  with infinitesimally thin cylindrical slices with their radius,  $r$ , perpendicular to the jet axis. A similar approach is used in the model of Chyży (1997). However, in this model the dynamical evolution and the radio luminosity of the entire cocoon depend on the geometrical shape and evolution of the volume elements. In the model of KA and KDA this is not the case and the identification of the  $\delta V_c$  with a specific geometrical shape does not alter their results.

The volume of a thin cylindrical slice of the cocoon is given by  $\delta V_c = \pi r_c^2 \delta z$ , where  $\delta z$  is the very small thickness of the slice along the jet axis. The radius of the slices,  $r_c$ ,

**Table 1.** Typical value ranges for the dimensionless constants in the dynamical model. This assumes  $0 \leq \beta \leq 2$  and  $1.3 \leq R_T \leq 6$  (e.g. Leahy & Williams 1984).

$c_1$	$c_3$	$c_4$	$c_6$	$c_7$
[1.6, 6.0]	[0.01, 0.3]	[0.6, 1.5]	[-1.5, 0.0]	[0.5, 0.8]

depends on their position along the jet axis,  $l$ , which I define in units of  $L_j$ , the length of one half of the entire cocoon (see Sect. 3.1). The outer edges of the slices form the cocoon boundary or contact discontinuity. Most FR II sources have cocoons of a relatively undistorted, ellipsoidal shape (e.g. Leahy et al. 1989). I therefore parameterise the cocoon boundary as

$$r_c = \alpha_o (1 - l^{\alpha_1})^{\alpha_2}, \quad (12)$$

where  $\alpha_o$ ,  $\alpha_1$  and  $\alpha_2$  can be determined from radio observations of the cocoon.

Following the observational results of Leahy & Williams (1984) and Leahy et al. (1989) KA and KDA used the aspect ratio,  $R_T$ , to characterise the geometrical shape of the cocoons of FR II sources. This ratio is defined as the length of one side of the cocoon measured from the radio core to the cocoon tip divided by its width measured half-way along this line. Using this definition it is straightforward to express  $\alpha_o$  in terms of  $R_T$  as

$$\alpha_o = \frac{L_j}{2R_T} \left[ 1 - \left( \frac{1}{2} \right)^{\alpha_1} \right]^{-\alpha_2}. \quad (13)$$

The dimensionless volume constant  $c_3$  now becomes

$$\begin{aligned} c_3 &= \pi \frac{\alpha_o^2}{L_j^2} \int_0^1 (1 - l^{\alpha_1})^{2\alpha_2} dl \\ &= \pi \frac{\alpha_o^2}{\alpha_1 L_j^2} B(2\alpha_2 + 1; 1/\alpha_1), \end{aligned} \quad (14)$$

where  $B(\mu; \nu)$  is the complete Beta-function.

Tab. 1 shows typical values for the dimensionless constants in the model.

### 3.4. Backflow

The cylindrical slices are injected into the cocoon at a time  $t_i$ . For simplicity I assume that the slices remain and thus move within the cocoon as entities afterwards. In other words, I neglect any mixing of material between slices and I also assume that the geometrical shape of the slices does not deviate from the initial thin cylinders. Numerical simulations (e.g. Falle 1994) show that the gas flow in the cocoon is rather turbulent, at least close to the hot spot region. It is likely that large-scale turbulent mixing in the cocoon leads to large distortions of the projected cocoon

shape as seen in radio observations. In this case, the regular cocoon shape described by Eq. (12) will be a poor representation of the ‘true’ cocoon shape. For such distorted sources it is unlikely that the model presented here will provide a good description. However, the simple picture of cylindrical slices may still represent the ‘average’ behaviour of the gas flow in more regularly shaped cocoons rather well.

The model is designed to constrain source and environment parameters using mainly the gradient of the radio surface brightness along the cocoon. Problems with this simplified model will therefore arise if the relativistic electrons in the cocoon are distributed efficiently by diffusion. In Sect. 6 I show that the diffusion of relativistic particles is unlikely to change their distribution on large scales. It is therefore reasonable to assume that the relativistic particles are effectively tied to the cocoon slice they were originally injected into.

Numerical simulations of the large scale structure of FRII sources strongly suggest that a backflow of material along the jet axis is established within the cocoon (e.g. Norman et al. 1982). The model describing the source dynamics predicts the growth of the cocoon to be self-similar and therefore the backflow within the cocoon should be self-similar as well. This suggests that the position of a slice of cocoon material injected into the cocoon at time  $t_i$  is given by  $l = (t_i/t)^{\alpha_3}$ , where  $\alpha_3$  governs the velocity of the backflow at a given position along the cocoon. In order for the model to be self-consistent, all  $\delta V_c$  have to add up to the total volume of the cocoon,  $V_c$ . Using Eqs. (2), (4), (5), (13) and (14) and replacing  $t_i/t$  by  $l^{1/\alpha_3} \equiv x$  an implicit Eq. for  $\alpha_3$  can be found from this integration;

$$\begin{aligned} & \frac{\alpha_1 \Gamma_c (5 - \beta)}{(9\Gamma_c - 4 - \beta)} B(2\alpha_2 + 1; 1/\alpha_1)^{-1} \\ &= \int_0^1 x^{c_4(\Gamma_c - 1)} (1 - x^{\alpha_1 \alpha_3})^{-2\alpha_2} dx \\ &= \frac{1}{\alpha_1 \alpha_3} B(1 - 2\alpha_2; [c_4(\Gamma_c - 1) + 1]/(\alpha_1 \alpha_3)). \end{aligned} \quad (15)$$

Note that this expression requires  $0 < \alpha_2 < 1/4$  and gives  $\alpha_3 \geq 0$ . For the values of the shape parameters used in Sect. 5 ( $\alpha_1 = 2$  and  $\alpha_2 = 1/3$ ) and  $\beta = 1.5$  I find  $\alpha_3 \sim 4.7$ . Note that  $\alpha_3 \rightarrow \infty$  for  $\alpha_2 \rightarrow 1/4$ .

The backflow velocity within the cocoon is given by

$$v_{\text{back}} = l \left( 1 - \frac{5 - \beta}{3} \alpha_3 \right) \dot{L}_j, \quad (16)$$

where a dot denotes a time derivative. In the rest frame of the host galaxy the backflow is observed to flow in the direction of the source core for  $v_{\text{back}} \leq 0$ . For  $v_{\text{back}} = 0$  the cocoon material is stationary in this frame and for positive values the backflow is strictly speaking not a ‘backflow’ but trailing after the advancing hot spot.

The backflow is fastest just behind the hot spot and decelerates along the cocoon. The deceleration implies a pressure gradient along the cocoon which may seriously violate the assumption made for the dynamical model of a constant pressure throughout the cocoon away from the hot spots. To estimate the magnitude of the pressure gradient I use Euler’s equation

$$\frac{dv_{\text{back}}}{dt} = -\frac{1}{\rho_c} \frac{dp(l)}{L_j dl}. \quad (17)$$

The density of the cocoon material,  $\rho_c$ , is given by

$$\begin{aligned} \rho_c &= \frac{Q_o \delta t_i}{(\gamma_j - 1) c^2 \delta V_c} \\ &= \frac{p_c(t_i)}{(\gamma_j - 1)(\Gamma_c - 1) c^2} P_{\text{hc}}^{(\Gamma_c - 1)/\Gamma_c} l^{c_4/\alpha_3}, \end{aligned} \quad (18)$$

where I assumed that the entire energy in the jet is transported in the form of kinetic energy of the flow with a bulk velocity corresponding to the Lorentz factor  $\gamma_j$ . With this, it is straightforward with the help of Eq. (16) to integrate Eq. (17) which yields the pressure along the cocoon as a function of  $l$ ;

$$\begin{aligned} \frac{p(l)}{p_c} &= 1 - \frac{(\alpha'_3 - 1)(3\alpha'_3 + 2 - \beta) P_{\text{hc}}^{(\Gamma_c - 1)/\Gamma_c}}{3(\gamma_j - 1)(\Gamma_c - 1)[2 + c_4/\alpha_3(1 - \Gamma_c)]} \\ &\quad \times \left( \frac{\dot{L}_j}{c} \right)^2 l^{2 + c_4/\alpha_3(1 - \Gamma_c)}, \end{aligned} \quad (19)$$

where  $\alpha'_3 = (5 - \beta)\alpha_3/3$  and I have used the condition  $p(0) = p_c$ . The mean advance speed of the cocoon of an FRII source,  $\dot{L}_j$ , is inferred from observations of lobe asymmetries to be in the range from 0.05 c (Scheuer 1995) to 0.1 c (Arshakian & Longair 2000). This is in good agreement with the predictions of the dynamical model used here (see KA). The ratio  $P_{\text{hc}}$  is usually of order 5 (see Eq. 7) and so even for only mildly relativistic bulk flow in the jet ( $\gamma_j \sim 2$ ) and large gradients in the backflow velocity, e.g.  $\alpha_3 \sim 10$ , Eq. (19) predicts  $0.28 \leq p(l)/p_c \leq 1.0$ . Note that for  $\gamma_j = 5$  the lower limit of this ratio increases to 0.82.

From this I conclude that the existence of a pressure gradient along the jet within the cocoon is required to decelerate the backflow of the cocoon material. However, the pressure varies only by a factor of a few at most along the entire length of the cocoon. This implies that within this limit the model is self-consistent.

#### 4. Comparison with observations

The model presented here depends on a large number of parameters. I assume that each volume element only contains the relativistic particle population and therefore  $\Gamma_c = \Gamma_B = 4/3$ . The other model parameters can be roughly grouped into

- geometrical parameters: the constants describing the cocoon shape  $\alpha_1$ ,  $\alpha_2$  and  $R_T$  and the orientation of the jet axis with respect to the Line-Of-Sight (LOS),  $\theta$ ,
- properties of the initial energy distribution of the relativistic electrons and/or positrons: the slope of the distribution,  $p$ , and the high energy cut-off,  $\gamma_{\max}$ ,
- properties of the source and its environment: the pressure within the cocoon,  $p_c$ , the age of the source,  $t$ , and the slope of the power law density distribution of the environment,  $\beta$ .

In the following I discuss the methods employed in comparing the model predictions with observations. Using these methods, I will then show that because of the nature of the model several degeneracies between model parameters exist. Eliminating these requires further assumptions to be made but also reduces the complexity of the parameter estimation.

#### 4.1. 2-dimensional comparison

A radio map of an FRII source is composed of pixels which contain information on the monochromatic radio surface brightness of the source,  $S_\nu(l'_i, y'_j)$ , at a given position  $(l'_i, y'_j)$  projected onto the plane of the sky. Here I use the *projected* distance along the jet axis,  $l'$ , and perpendicular to the jet,  $y'$ . Both are measured in units of the projected length of the cocoon,  $L'_j$ . In optically thin conditions generally present in radio source lobes this projection corresponds to a LOS integral of the synchrotron emissivity,  $\epsilon_\nu$ , through the 3-dimensional source at each pixel location. Following the analysis in Sects. 3.1 and 3.2,  $\epsilon_\nu$  is only a function of the unprojected dimensionless distance from the core measured along the jet axis,  $l$ , for a given set of the eight source and environment parameters. Using the model described above, it is therefore possible to construct ‘virtual radio maps’ for a given set of model parameters by projecting the 3-dimensional model onto the plane of the sky. Since a radio source is in general viewed with its jet axis at an angle  $\theta$  to the LOS, the value of  $l$ , and therefore that of  $\epsilon_\nu$ , changes along the path of the LOS integral. Also, the distance from the core to the tip of the cocoon measured on an observed radio map,  $L'_j$ , is not equal to the physical size of the cocoon,  $L_j = L'_j / \sin \theta$ . This, of course, also implies that the aspect ratio of the cocoon,  $R'_T$ , measured in the observed map is smaller than the ‘real’ value  $R_T = R'_T / \sin \theta$ , i.e. radio sources appear ‘fatter’ than they really are. All these projection effects have to be taken into account when comparing virtual radio maps resulting from these models to observations.

The surface brightness is calculated at a frequency  $\nu$  which is given by the observing frequency in the frame of the observer,  $\nu'$ , and the redshift of the source, i.e.  $\nu = (1+z)\nu'$ . Finally, to account for cosmological effects the result

of the LOS integration must be multiplied by  $(1+z)/D_L^2$ , where  $D_L$  is the luminosity distance to the source.

The model map can be calculated at arbitrary resolution. However, before comparing the result with the observed map it must be convolved with the beam of the radio telescope used for the observations. This was done assuming a 2-dimensional Gaussian shape for the telescope beam.

Once a virtual map is compiled for a set of model parameters this map can be compared pixel by pixel to a map resulting from observations of an FRII radio source using a  $\chi^2$ -technique,

$$\chi_\nu^2 = \sum_i^n \sum_j^m \frac{[S_\nu(l'_i, y'_j) - M_\nu(l'_i, y'_j)]^2}{\sigma_\nu^2}. \quad (20)$$

Here,  $S_\nu$  is the measured monochromatic surface brightness with rms error  $\sigma_\nu$  and  $M_\nu$  is the model prediction.

It is then possible to find the best-fitting model by varying the model parameters and thereby minimising the resulting  $\chi^2$ -difference between virtual and observed map. The minimisation routine uses a n-dimensional downhill simplex method (Press et al. 1992), where n is the number of model parameters to be fitted. The minimisation can be done separately for the two halves of each cocoon since the model describes one jet and the associated half of the cocoon. Although in principle the minimisation can be done with one observed map at a single observing frequency, the constraints on the model parameters are improved by using two maps at two different frequencies. In this case the  $\chi^2$ -differences resulting from the two maps are simply added together. In principle this is equivalent to compiling spectral index maps from two observed maps and comparing these with the model predictions. However, using the two maps directly has the advantage that pixels below the rms limit in one map but not in the other are not entirely lost for the fitting procedure. Furthermore, information on the absolute surface brightness in a given location is not contained in a spectral index map. The model would have to be normalised ‘by hand’ and the various possibilities to do this would lead to ambiguities in the estimation of model parameters. In Sec. 5 I use two individual maps at two frequency for each source.

Using the best-fitting model parameters  $p_c$  and  $t$ , the energy transport rate of the jet,  $Q_o$ , and the parameter combination  $\rho_o \alpha_o^\beta$  describing the density distribution in the source environment can be calculated from Eqs. (2) and (3).

Preliminary results using this comparison technique applied to radio observations of Cygnus A was presented in Kaiser (2000). In Sect. 5 this analysis is extended to also include 3C 219 and 3C 215.

**Table 2.** Model parameters of the fiducial model (see text).

fixed parameters	$p_c/\text{J m}^{-3}$	$5 \cdot 10^{-11}$
	$t/\text{years}$	$10^7$
	$\theta/\text{degrees}$	60
	$R_T$	2.3
	$\alpha_1$	2
	$\alpha_2$	1/3
	$p$	2.0
	$\gamma_{\text{max}}$	$10^{4.5}$
	$\beta$	1.5
	$L_j/\text{kpc}$	100
derived parameters	$B/\mu\text{G}$	130
	$Q_o/W$	$4.3 \cdot 10^{38}$
	$\rho_o a_o^\beta/\text{kg m}^{-1.5}$	$8.8 \cdot 10^7$
	$L'_j/\text{kpc}$	86.6
	$R'_T$	2
	$\alpha_3$	4.7

#### 4.2. 1-dimensional comparison

The 2-dimensional comparison method described in the previous section requires a ray-tracing algorithm for the projection of the 3-dimensional model. For many maps of radio sources the number of pixels are so large that this method can become computationally very expensive. Furthermore, for maps of lower resolution the cocoon may not be resolved in the direction perpendicular to the jet axis. In such maps the surface brightness gradient along the jet axis can be extracted by taking a cut through the map along the line connecting the source core and the radio hot spot in the cocoon on one side. This yields a 1-dimensional curve of surface brightness as a function of projected distance from the source core,  $S_\nu(l')$ . The off-axis pixels will not add much information. The function  $S_\nu(l')$  can then be compared with the model predictions and a best-fitting model may be found using two maps at two observing frequencies as outlined in the 2-dimensional case. This 1-dimensional comparison involves a much smaller number of pixels for which a model prediction must be calculated than the 2-dimensional method.

#### 4.3. Model parameters

To study the influence of the individual model parameters on the surface brightness distribution, I define a fiducial model with a set of fixed model parameters given in Tab. 2. These model parameters imply a magnetic field just behind the hot spot of 13 nT or 130  $\mu\text{G}$ . The highest frequency of the emitted synchrotron spectrum is then  $\sim 300$  GHz which is close to the usually assumed high frequency cut-off in the spectrum of radio galaxies in minimum energy arguments (e.g. Miley 1980). The density parameter  $\rho_o a_o^\beta = 8.8 \cdot 10^7 \text{ kg m}^{-1.5}$  which corresponds to a central

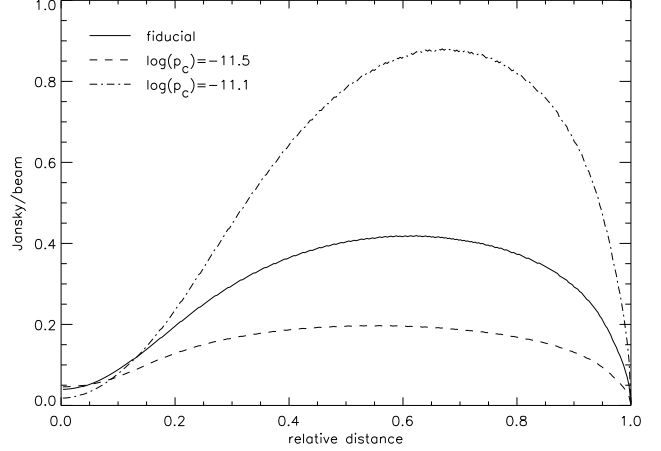


**Fig. 1.** The influence of the cocoon pressure on the radio surface brightness along the jet axis. All curves are plotted for the parameters of the fiducial model except for a variation in the cocoon pressure. The relative distance from the core of the source is given in units of  $L'_j = 86.6$  kpc (see text). The surface brightness is plotted as it would be extracted by an observer from a map of a source at redshift  $z = 0.1$ .

density of  $5 \cdot 10^{-22} \text{ kg m}^{-3}$  or 0.3 particles per  $\text{cm}^{-3}$  if  $a_o = 10$  kpc. I also assume that the jet of the sources is 100 kpc long and is viewed at an angle of  $\theta = 60^\circ$  to the line of sight. This implies that it would be observed to have a length of  $L'_j = 86.6$  kpc corresponding to  $31.2''$  at a redshift  $z = 0.1$ . For a measured  $R'_T = 2$  the aspect ratio of the cocoon is  $R_T = 2.3$  for the assumed viewing angle.

For simplicity and ease of comparison I use the 1-dimensional model which only predicts the surface brightness distribution along the jet axis (see previous Sect.). The variation of the model predictions with varying parameters for the 2-dimensional case are essentially similar but the differences between maps are more difficult to visualise.

The solid line in Fig. 1 shows  $S_\nu(l)$  at  $\nu' = 1.5$  GHz assuming a pixel size of  $0.3'' \times 0.3''$ , corresponding to  $0.8 \text{ kpc} \times 0.8 \text{ kpc}$  for  $z = 0.1$ , appropriate for a telescope beam of  $1.2''$  FWHM. For simplicity and in contrast to the 2-dimensional comparison method the averaging effects of the observing beam which extends over four pixels on the curve was not taken into account. In any case, in this Sect. the only interest is in gross trends of the model predictions when the model parameters are varied and the effective smoothing of the beam on the already rather smooth curve is small. A continuous curve is shown, since the pixel size is small compared to the scale of the plot. The length of the cocoon corresponds to more than 100 pixels. As pointed out in Sect. 3.2, the emission of the hot spot is not modeled in the approach presented here. The cocoon surface brightness shown in this and the following figures is caused by the cocoon material only after it has passed



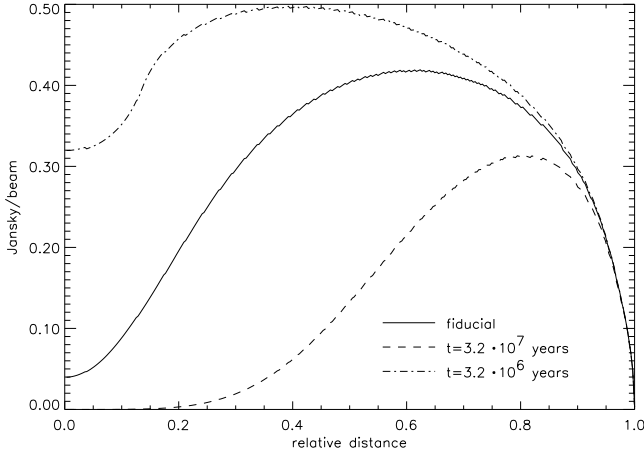


**Fig. 2.** The influence of the source age on the radio surface brightness. All model parameters as in Fig. 1 except for a variation in the source age.

through the hot spot region. The emission from the hot spot will in general dominate the total emission from the end of the cocoon at  $l \rightarrow 1$ . In a comparison with observed maps the predictions of the model can therefore not be used in this region.

Also shown in Fig. 1 are the results for the same model with a higher and lower cocoon pressure. In the model the strength of the magnetic field and the energy density of the relativistic particles in the cocoon is tied to the cocoon pressure. A higher pressure therefore causes a higher peak of the surface brightness distribution. However, the increased synchrotron energy losses of the relativistic electrons also lead to a stronger gradient of the distribution towards the core of the source, i.e. the older parts of the cocoon.

In Fig. 2 the effects of the source age on the distribution of  $S_\nu(l)$  is shown. The population of relativistic particles at a given relative distance,  $l$ , from the core of the source has spent more time in the cocoon in an old source compared to a young source. This implies stronger energy losses and the peak of the surface brightness distribution is therefore located closer to the hot spot in an old source. Furthermore, in an observation with a given detectable threshold of  $S_\nu(l)$  a larger fraction of the cocoon of a young source will be visible than of an older source.

The same source viewed at different angles of the jet axis to the LOS, as shown in Fig. 3, results in a scaling of the surface brightness similar to the effects of changing the cocoon pressure. Note however, that the overall normalisation of  $S_\nu(l)$  depends sensitively on the value of the cocoon pressure. The effects of a higher pressure also include a steepening of  $S_\nu(l)$  starting from the peak of this function towards the source core (Fig. 1). This is not seen for variations of the viewing angle (Fig. 3). In practice therefore, the best-fitting values for the cocoon

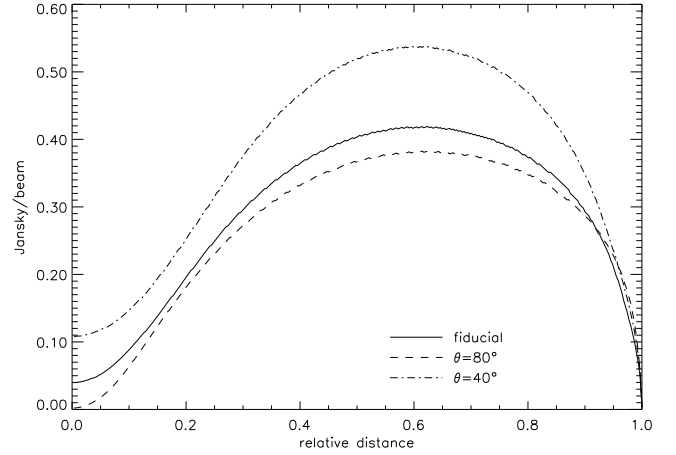


**Fig. 3.** The influence of the viewing angle on the radio surface brightness. All model parameters as in Fig. 1 except for a variation in  $\theta$ . Note that the measured length of the cocoon,  $L_j^l$ , changes from 86.6 kpc for the fiducial model to 98.5 kpc for  $\theta = 80^\circ$  and 64.3 kpc for  $\theta = 40^\circ$ .

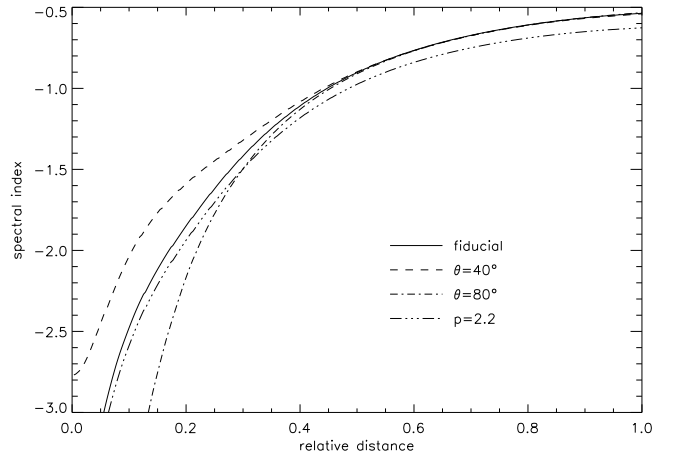


**Fig. 4.** Spectral index between 1.5 GHz and 5 GHz for the fiducial model and models with varying viewing angle,  $\theta$ , and slope of the initial energy spectrum of the relativistic particles,  $p$ . All other model parameters as in Fig. 1.

pressure is set mostly by the overall surface brightness of the cocoon while the viewing angle is mainly determined by the behaviour of  $S_\nu(l)$  close to the core.

Fig. 5 summarises the effects of the remaining model parameters on the surface brightness distribution. Changing the aspect ratio of the cocoon,  $R_T$ , results in a scaling of  $S_\nu(l)$  very similar to the effects of a changing viewing angle,  $\theta$ . Decreasing  $\alpha_2$  leads to the end of the cocoon to become more blunt which in turn implies a lower value of  $\alpha_3$ , i.e. a slower backflow within the cocoon (Eqs. 16 and 16). This is analogous to an older particle population at a given distance from the hot spot and the resulting surface brightness distribution is similar to that of an older

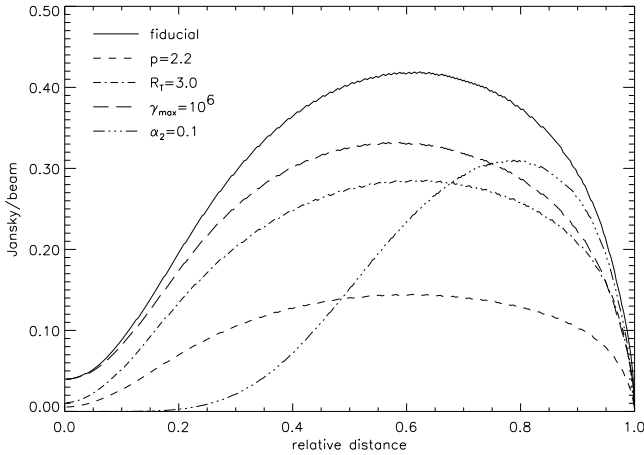


**Fig. 5.** Effects of other model parameters on the radio surface brightness. Model parameters are as in Fig. 1 unless otherwise indicated in the legend.

source. Changing the second shape parameter  $\alpha_1$  has similar effects as that of a variation of  $\alpha_2$  and is therefore not shown.

The main effects of changing the slope,  $p$ , and the high energy cut-off of the initial energy distribution of the relativistic electrons,  $\gamma_{\max}$ , is a change in the scaling of  $S_\nu(l)$  (see Fig. 5). This is caused by the dependence of the normalisation of the energy spectrum on  $p$  and  $\gamma_{\max}$ , Eq. (11). Both scaling effects are similar to the effects of a variation of the viewing angle,  $\theta$ . The effect of a steeper energy spectrum also causes an off-set in the distribution of the spectral index as a function of  $l$  as shown in Fig. 4. However, in the cocoon region closest to the source centre and least influenced by the hot spot emission, this effect is small compared to that of a variation of the viewing angle,  $\theta$ .

Finally, a different value of the slope of the gas density distribution in the source environment,  $\beta$ , has a negligible effect on  $S_\nu(l)$ . The relevant curves for  $\beta = 1$  and  $\beta = 2$  are indistinguishable from that for  $\beta = 1.5$  shown in Figs. 1 to 5.

#### 4.4. Degeneracy of parameters

Both,  $\alpha_1$  and  $\alpha_2$ , control how pointed the shape of the cocoon is. The ends of the cocoon are dominated by the emission from the hot spots which are not part of the model. Furthermore, if the jet direction is not stable over the lifetime of the source, they may at times advance ahead of the rest of the cocoon which distorts the cocoon shape. This has been referred to as the ‘dentist drill’ effect (Scheuer 1982). In the previous Sect. (see also Eq. 16) it was already shown that changing  $\alpha_1$  and/or  $\alpha_2$  results in a change of the profile and magnitude of the backflow in the cocoon. This in turn causes changes to the surface brightness pro-

files similar to changes of the source age. For these reasons the model cannot provide strong constraints on either of these parameters, at least not independent of the source age. Therefore I set in the following  $\alpha_1 = 2$  and  $\alpha_2 = 1/3$ .

The surface brightness distribution predicted by the model is almost independent of the slope of the density profile of the external medium,  $\beta$ . I therefore set  $\beta = 1.5$  without influencing the model results significantly. Note that because of Eq. (16) this then also implies a fixed value for  $\alpha_3 = 4.8$ . This may seem a rather significant restriction of the model but as was shown in the previous Sect.  $\alpha_1$  or  $\alpha_2$ , through their influence on  $\alpha_3$ , and the age of the source,  $t$ , are degenerate model parameters. In the absence of geometrical constraints on  $\alpha_1$  or  $\alpha_2$ , setting them to reasonable values allows the determination of the source age from the fitting method. The ages derived from the model will therefore always depend somewhat on the choice for the source geometry.

The slope of the initial energy distribution of the relativistic particles,  $p$ , mainly influences the spectral index distribution in the cocoon. Observations suggest that  $2 \leq p \leq 3$  and the model is therefore restricted to values in this range. It follows that the model is rather insensitive to the exact value of the high energy cut-off of the distribution,  $\gamma_{\max}$ . A value of  $\gamma_{\max}$  much smaller than the  $10^{4.5}$  used in the fiducial model will, in addition to a change of the overall scaling, cause the emission region to shorten along the jet axis at a given observing frequency. However, because the highest frequency of the synchrotron radiation of the cocoon,  $\nu_{\max}$ , depends on  $\gamma_{\max}^2$  a small value of the high energy cut-off also implies a significantly smaller  $\nu_{\max}$ . Values substantially below  $\nu_{\max} \sim 100$  GHz, which is assumed, here are unlikely in view of observations. I therefore set  $\gamma_{\max} = 10^{4.5}$ .

As was pointed out above, the effects of varying the initial slope of the energy distribution of the relativistic particles,  $p$ , are small in general. In Sect. 5 the 1 and 2-dimensional comparison methods are applied to observations of three FR II-type radio sources. It is shown there that in almost all cases the best-fitting model parameters for the 2-dimensional method require  $p$  to be close to 2. To prevent the degeneracy between  $p$  and  $\theta$  to influence the model fits in the 1-dimensional method which involves fewer degrees of freedom, I set  $p = 2$  in this case.

Finally, the degeneracy between  $R_T$ , the width of the cocoon, and the viewing angle,  $\theta$ , is resolved by determining the projected cocoon width  $R'_T$  from the observed map and use  $R_T = R'_T / \sin \theta$  in the model calculations.

Using these additional assumptions, the number of model parameters which are fitted by comparison to the observations decreases to four: The pressure in the cocoon,  $p_c$ , the source age,  $t$ , the viewing angle,  $\theta$ , and the initial slope of the energy distribution of the relativistic particles,  $p$ . In the case of the 1-dimensional comparison method  $p$  is fixed to a value of 2.

## 5. Application to Cygnus A, 3C 219 and 3C 215

To test the model predictions for the source environment against direct X-ray observations over a range of different viewing angles, the radio data of three different FRII-type objects are used: the narrow-line radio galaxy Cygnus A, the broad-line radio galaxy 3C 219 and the radio-loud quasar 3C 215. According to orientation-based unification schemes of the various sub-classes of radio-loud AGN (e.g. Barthel 1989), the viewing angle,  $\theta$ , of Cygnus A should be greater than those of 3C 219 and 3C 215. Furthermore, 3C 219 and 3C 215 were selected because of their rather irregular radio lobe structure. The model is based on a very regular geometrical shape of the cocoon, Eq. (12), and using 3C 219 and 3C 215 it is possible to estimate to what extent this restriction limits the applicability of the model.

Note, that results of the model fitting for Cygnus A are presented in 8 and 9 only at one frequency. However, the model fits are always obtained for all sources using two maps at two different frequencies.

### 5.1. Cygnus A

For this source at  $z = 0.056$  I used raw data from the VLA archive at 1.8 GHz and 5 GHz. The lower frequency observations were made in August/September 1987 in A-array and the 5 GHz data were obtained in January 1984 in B-array. A detailed analysis of these and other observations of Cygnus A can be found in Carilli et al. (1991). Standard calibration and self-calibration was performed using the software package AIPS. This resulted in two radio maps with comparable angular resolution of  $1.3''$  at the two observing frequencies. The CLEAN components were restored in maps with an individual pixel size of  $0.3'' \times 0.3''$ . The map at 1.8 GHz with the hot spot emission removed (see below) is shown in the upper panel of Fig. 6. The rms noise in the maps is  $0.03 \text{ Jy beam}^{-1}$  at 1.8 GHz and  $0.006 \text{ Jy beam}^{-1}$  at 5 GHz. All pixels in the maps with a surface brightness below  $5\sigma$  were discarded for the 2-dimensional comparison method. In the case of the 1-dimensional method only pixels below  $3\sigma$  were neglected. The surface brightness distribution along the jet axis,  $S_\nu(l)$ , for the 1-dimensional method was obtained for both radio lobes along a cut from the core of the source to the eastern and western hot spot respectively.

Since the hot spot emission is not modeled, it has to be removed from the maps and the 1-dimensional cuts. In the maps an aperture centered on the surface brightness peak in each lobe and with a radius of  $2.6''$  corresponding to twice the beam width is removed (see Fig. 6). In the western lobe the bright secondary hot spot (Carilli et al. 1991) and the bright ridge connecting this hot spot with the main one are also removed. For the 1-dimensional method, the distance of the hot spot to the edge of the lobe,  $\Delta l$ , was estimated as the distance of the maximum of  $S_\nu(l)$  to

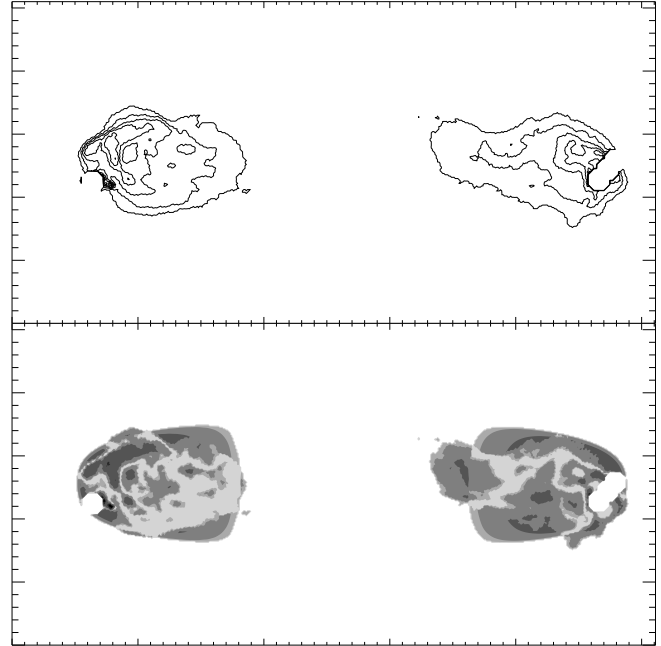


**Fig. 6.** The 2-dimensional comparison method applied to Cygnus A. The upper panels shows the observed map at 1.8 GHz. Contours are increasing linearly in steps of  $0.43 \text{ Jy beam}^{-1}$ , starting at  $0.14 \text{ Jy beam}^{-1}$ , the  $5\text{-}\sigma$  noise level, to a peak just above  $3 \text{ Jy beam}^{-1}$ . The map is rotated by about  $20^\circ$  clockwise compared to the true position angle. The lower panel shows the  $\chi^2$ -deviation of the best-fitting models. The filled contours show regions where  $\chi^2 = 0$  (white),  $0 < \chi^2 \leq 1$ ,  $1 < \chi^2 \leq 2$ ,  $2 < \chi^2 \leq 10$ ,  $10 < \chi^2 \leq 50$ ,  $50 < \chi^2 \leq 100$  and  $\chi^2 > 100$  (black). Note that the best-fitting model for the eastern and western lobes are not identical (see Table 3). The results for both lobes are presented together for ease of comparison. The best-fitting model is obtained by fitting the 1.8 GHz map presented here and simultaneously the 5 GHz data (see Fig. 7)

the last point at which this function has a value above  $3\sigma$  in the direction away from the source core. To remove the contribution of the hot spots to  $S_\nu(l)$ , all pixels within  $2\Delta l$  of the edge of the lobe were neglected in the following 1-dimensional comparison process.

The spatial resolution of the radio maps of Cygnus A is comparatively high. The  $1.3''$  angular resolution corresponds to a spatial resolution of about 1.9 kpc. For many sources, particularly at high redshift, maps of such high quality are not available. In order to estimate the effects of a lower angular and therefore lower spatial resolution, I also convolved the two maps of Cygnus A with a Gaussian beam of  $5''$  FWHM. In the case of the 2-dimensional method the radius of the aperture used to remove the hot spot emission was fixed to  $5''$ . For the 1-dimensional method, the surface brightness distribution along the jet axis was extracted from these lower resolution maps in the same way as in the higher resolution case. Note that

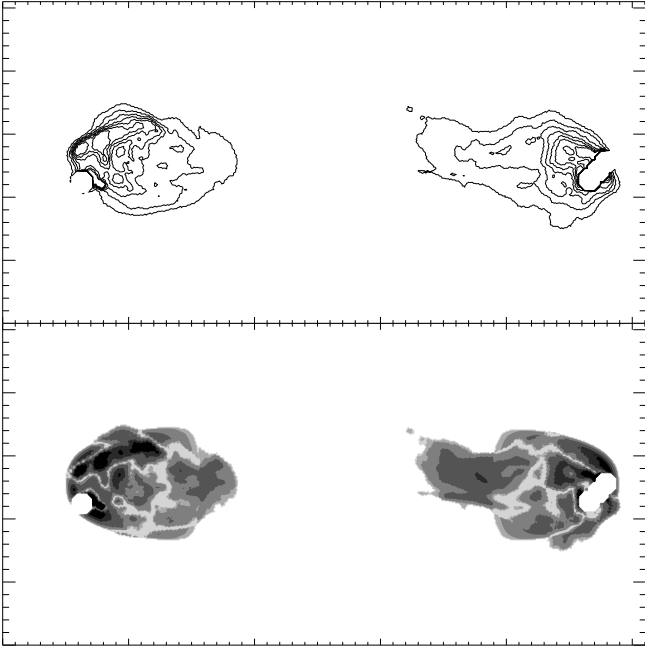


**Fig. 7.** Same as Fig. 6 but at 5 GHz. The contour levels in the upper panel are spaced linearly in steps of  $0.12 \text{ Jy beam}^{-1}$  starting at  $0.03 \text{ Jy}$ , the  $5 - \sigma$  level, to  $0.76 \text{ Jy beam}^{-1}$ . Higher contours are omitted for clarity. The  $\chi^2$ -contours are as in Fig. 6.

the emission of the hot spots is smeared out over a larger area in the low resolution maps. To avoid any bias from the enhanced emission of the hot spot region I used the higher value of  $2\Delta l$  obtained from the low resolution maps in both, the high and low resolution, 1-dimensional comparison.

### 5.1.1. The eastern lobe

The eastern lobe of Cygnus A is covered by 46.6 independent telescope beams along the jet while in the widest part there are 22.2 beams across. In the lower resolution maps these numbers decrease to 12.9 and 6.1, respectively. Note, that only a fraction of the lobes has an observed surface brightness above the rms limits, i.e. they do not extend all the way from the hot spots to the core in the observations. This implies that the model fits are based on regions covering less area than the theoretical extend of the cocoons. For both resolutions I find an axial ratio,  $R'_T$ , of 2.1 at the point where the lobe is widest from the 2-dimensional maps. The length of the lobe,  $L'_j$ , is  $64.4''$  for the low resolution map and  $60.6''$  for the high resolution map. The prediction of the best-fitting model in comparison with the observations is shown in the lower panels of Figs. 6 and 7 for the 2-dimensional method and in Figs. 8 and 9 for the 1-dimensional method at 1.8 GHz. The 5 GHz data is not shown for the 1-dimensional method but is similar to the result at 1.8 GHz. The parameters of the best-fitting

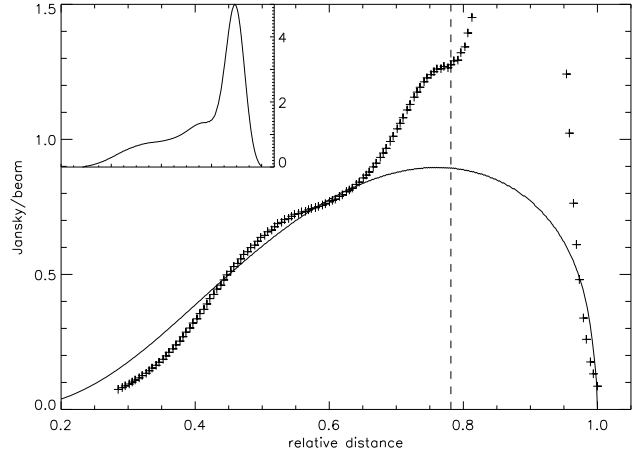


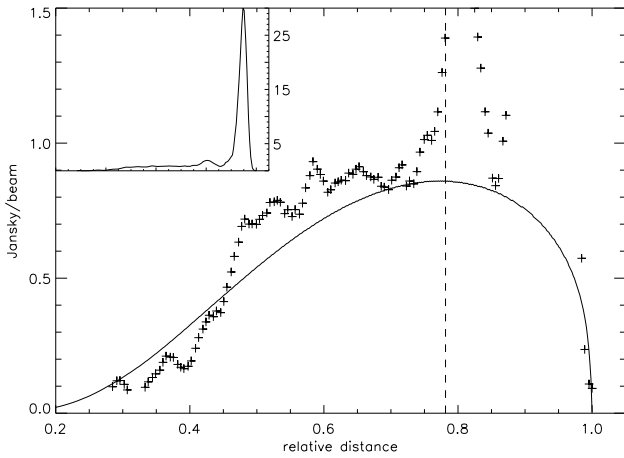
**Fig. 8.** Comparison of the predicted surface brightness distribution along the cocoon with the low resolution observations of the eastern lobe of Cygnus A. The crosses show the value of  $S_\nu(l)$  at 1.8 GHz along the jet axis taken from the VLA map convolved with a  $5''$  Gaussian beam. The solid line shows the best-fitting model with the model parameters given in table 3. Only data points left of the dashed line located at  $2\Delta l$  from the tip of the cocoon (see text) were used in the fitting procedure to avoid the contribution of the hot spot. The entire observed range of  $S_\nu(l)$  including the peak of the hot spot is shown in the inset.

models are given in table 3. The errors on these and for all the following model fits are estimated using the boot-strap method (e.g. Press et al. 1992). It is not possible to calculate error estimates using the  $\chi^2$ -values derived in the minimisation procedure directly as the values of the surface brightness in neighboring pixels are not independent. Roughly 2000 data sets were created by drawing data with replacement from the original set. The same minimisation procedure as in the original model fitting was then applied to them and the error given in the table is the  $1\sigma$  limit on the respective model parameters.

Even after subtracting the contribution of the hot spot the deviations of the model from the observations are large. The fact that the model fit is poorer at 5 GHz is mainly caused by the smaller rms noise of the observed 5 GHz map. As expected, the model cannot fit structures which appear as discrete surface brightness enhancements in the maps. This is particularly clear in the case of the bright arc seen just behind the hot spot in radio maps of the eastern lobe (see Figs. 6 and 7) which also causes the secondary peak in  $S_\nu(l)$  at about  $l = 0.83$  (see Fig. 9). Although convolving the maps with a larger beam ‘draws’ some flux from the hot spot into the arc mentioned above, the results for the two different resolutions are very similar for both comparison methods. At both frequencies the observed maps show a concentration of the radio emission towards the centres of both lobes. This region is also ex-

**Table 3.** The best-fitting model parameters from the 1 and 2-dimensional comparison methods.

			$\log(p_c/\text{Jm}^{-3})$	$t/10^6\text{years}$	$\theta/\text{degrees}$	$p$
Cygnus A, eastern lobe	5" resolution	2-D	$-11.01^{+.06}_{-.01}$	$14.5^{+2.9}_{-1.3}$	$71^{+16}_{-29}$	$2.00^{+.07}_{-.00}$
		1-D	$-11.08^{+.04}_{-.02}$	$13.8^{+4.0}_{-0.9}$	$79^{+10}_{-18}$	...
	1.3" resolution	2-D	$-10.90^{+.02}_{-.05}$	$13.8^{+2.5}_{-.9}$	$87^{+3}_{-11}$	$2.07^{+.01}_{-.07}$
		1-D	$-11.07^{+.05}_{-.08}$	$14.5^{+5.5}_{-1.3}$	$84^{+6}_{-28}$	...
Cygnus A, western lobe	5" resolution	2-D	$-10.85^{+.04}_{-.25}$	$15.2^{+16.5}_{-1.7}$	$75^{+14}_{-56}$	$2.13^{+.04}_{-.13}$
		1-D	$-11.01^{+.05}_{-.02}$	$15.9^{+7.1}_{-2.4}$	$83^{+7}_{-21}$	...
	1.3" resolution	2-D	$-10.87^{+.05}_{-.11}$	$17.4^{+3.6}_{-2.6}$	$82^{+2}_{-4}$	$2.10^{+.06}_{-.1}$
		1-D	$-11.09^{+.08}_{-.13}$	$15.2^{+6.7}_{-2.6}$	$79^{+11}_{-25}$	...
3C 219	4.3" resolution	2-D	$-12.12^{+.09}_{-.04}$	$34.8^{+.8}_{-7.8}$	$59^{+12}_{-6}$	$2.03^{+.09}_{-.01}$
		1-D	$-11.91^{+.03}_{-.08}$	$44.8^{+17.0}_{-9.2}$	$65^{+24}_{-14}$	...
3C 215	1.9" resolution	2-D	$-12.20^{+.39}_{-.37}$	$35.6^{+23.4}_{-22.1}$	$31^{+32}_{-21}$	$2.22^{+.28}_{-.22}$
		1-D	$-12.38^{+.08}_{-.06}$	$38.1^{+9.9}_{-20.7}$	$43^{+57}_{-5}$	...

**Fig. 9.** Comparison of the predicted surface brightness distribution along the cocoon with the high resolution observations of the eastern lobe of Cygnus A. The data is taken from the unconvolved VLA map. As in Fig. 8 the solid line shows the best-fitting model and only data left of the dashed line was used in the fitting procedure.

tended a long way along the jet axis, particularly in the western lobe (see following section). In Figs. 6 and 7 it is clear that the model cannot fit this concentration properly. The very smooth lobes of the model are ‘fatter’ than the observed lobes further away from the hot spots and do not extend as far back as the observations indicate. This is particularly striking in the western lobe at 5 GHz (see Fig. 7). This clearly illustrates the limitations of the model

assumption of a smooth shape of the cocoon and a regular backflow within the cocoon. The large uncertainty of the viewing angle,  $\theta$ , is caused by the model mainly depending on  $\sin \theta$  which changes only by a factor 1.2 within the estimated errors. This is comparable to the uncertainties of the other model parameters.

Using Eqs. (2) and (3) The power of the jet,  $Q_o$ , and the central value of the density distribution of the gas surrounding Cygnus A,  $\rho_o$ , are calculated. The results are given in Table 4. Here I assume that the core radius of the environmental density distribution in Eq. (1) is given by  $a_o = 24$  kpc. The viewing angle  $\theta$  is inferred from the flux ratio of the jet to the counter-jet in the two lobes of Cygnus A (Hardcastle et al. 1999). This assumes that the two jets are identical and that the observed flux ratio is entirely due to relativistic beaming effects. Furthermore, a constant bulk velocity within the jets,  $v_j$ , is assumed and set to  $0.62 c$ . Variations of  $v_j$  across the source and asymmetries between the two jet sides will significantly influence the estimate for  $\theta$ . However, the model is consistent with the estimate given by Hardcastle et al. (1999).

The observed central density of source environment given in Table 4 is derived from X-ray observations ROSAT of the hot gas surrounding Cygnus A Hardcastle & Worrall (2000). For this, the prescription of Birkinshaw & Worrall (1993) for the conversion of central surface brightness to central proton density was used. The core radius,  $a_o$  was estimated by Hardcastle & Worrall (2000) from the X-ray observations and I use their value,  $a_o = 24$  kpc, in converting from the density parameter  $\rho_o a_o^\beta$  given by the model to  $\rho_o$ . The value thus found from

**Table 4.** Properties of the source environment derived from the best-fitting model parameters in comparison with observations. For the determination of  $\rho_o$  the core radii of Hardcastle & Worrall (2000) inferred from X-ray observations were used. These are  $a_o = 24$  kpc for Cygnus A,  $a_o = 140$  kpc for 3C 219 and  $a_o = 204$  kpc for 3C 215.

			$\theta/\text{degrees}$	$Q_o/W$	$\rho_o/\text{kgm}^{-3}$	$\rho_o/\text{cm}^{-3}$
Cygnus A, eastern lobe	5" resolution	2-D	$71^{+16}_{-29}$	$6.2^{+2.9}_{-.2} \cdot 10^{38}$	$1.7^{+1.9}_{-.3} \cdot 10^{-23}$	$9.9^{+11}_{-1.7} \cdot 10^{-3}$
		1-D	$79^{+10}_{-18}$	$5.3^{+.3}_{-.7} \cdot 10^{38}$	$1.3^{+1.1}_{-.1} \cdot 10^{-23}$	$7.4^{+6.1}_{-.9} \cdot 10^{-3}$
	1.3" resolution	2-D	$87^{+3}_{-11}$	$6.5^{+.4}_{-1.3} \cdot 10^{38}$	$1.9^{+.6}_{-.3} \cdot 10^{-23}$	$1.1^{+.4}_{-.2} \cdot 10^{-2}$
		1-D	$84^{+6}_{-28}$	$4.2^{+.5}_{-.7} \cdot 10^{38}$	$1.4^{+1.6}_{-.4} \cdot 10^{-23}$	$8.4^{+9.4}_{-2.0} \cdot 10^{-3}$
Cygnus A, western lobe	5" resolution	2-D	$75^{+14}_{-56}$	$1.1^{+.6}_{-.4} \cdot 10^{39}$	$2.9^{+22}_{-.6} \cdot 10^{-23}$	$1.7^{+13}_{-.4} \cdot 10^{-2}$
		1-D	$83^{+7}_{-21}$	$6.7^{+.5}_{-1.3} \cdot 10^{38}$	$2.1^{+2.8}_{-.9} \cdot 10^{-23}$	$1.2^{+1.7}_{-.5} \cdot 10^{-2}$
	1.3" resolution	2-D	$82^{+2}_{-4}$	$7.3^{+2.1}_{-2.4} \cdot 10^{38}$	$3.6^{+.8}_{-.6} \cdot 10^{-23}$	$2.1^{+.5}_{-.3} \cdot 10^{-2}$
		1-D	$79^{+11}_{-25}$	$5.1^{+.7}_{-1.2} \cdot 10^{38}$	$1.7^{+2.4}_{-.7} \cdot 10^{-23}$	$9.8^{+14}_{-4.2} \cdot 10^{-3}$
Cygnus A	observed		76	...	$2.4 \cdot 10^{-23}$	$1.4 \cdot 10^{-2}$
3C 219	4.3" resolution	2-D	$59^{+12}_{-6}$	$1.6^{+.8}_{-.1} \cdot 10^{38}$	$2.9^{+.4}_{-1.3} \cdot 10^{-25}$	$1.7^{+.2}_{-.7} \cdot 10^{-4}$
		1-D	$65^{+24}_{-14}$	$1.9^{+.1}_{-.3} \cdot 10^{38}$	$7.4^{+5.3}_{-3.8} \cdot 10^{-25}$	$4.3^{+3.2}_{-2.2} \cdot 10^{-4}$
3C 219	observed		32	...	$9.2 \cdot 10^{-24}$	$5.4 \cdot 10^{-3}$
3C 215	1.9" resolution	2-D	$31^{+32}_{-21}$	$6.7^{+37}_{-3.5} \cdot 10^{38}$	$1.5^{+3.0}_{-1.2} \cdot 10^{-25}$	$8.8^{+18}_{-7.3} \cdot 10^{-5}$
		1-D	$43^{+57}_{-5}$	$3.0^{+.6}_{-.1} \cdot 10^{38}$	$8.2^{+6.4}_{-7.1} \cdot 10^{-26}$	$4.8^{+3.8}_{-4.1} \cdot 10^{-5}$
3C 215	observed		32	...	$9.6 \cdot 10^{-24}$	$5.6 \cdot 10^{-3}$

the best-fitting model agrees within the error with the X-ray observations.

### 5.1.2. The western lobe

The western lobe of Cygnus A is covered by 53.5 independent beams along the jet and 23.2 beams at the widest point perpendicular to the jet. For the lower resolution maps I find 14.6 and 6.3 beams, respectively. Similar to the eastern lobe the observed emission does not extend all the way from the hot spot to the core and so the model fit is based on a smaller area. From the 2-dimensional maps I find  $R'_T = 2.3$  for the widest part of the lobe and the length of the lobe is 73.0" and 69.5" for the low and high resolution case respectively. The best-fitting models for the two different resolutions again agree well. The models yield an age for the western lobe somewhat higher than that of its eastern counterpart (see Table 3) which is mainly caused by its greater length. However, the pressure within the cocoon is remarkably similar in both lobes. This implies also good agreement between the estimates for the jet power and the density of the source environment between the two sides of Cygnus A (Table 4).

### 5.2. 3C 219

For 3C 219 at  $z = 0.1744$  VLA maps at 1.5 GHz in B-array and 4.9 GHz in C-array were used. The observations were taken in October and December 1998 by Dennett-Thorpe et al. (in preparation) who also performed standard reduction on the data set using AIPS. The resolution of the resulting maps is roughly 4.3" and the rms noise is  $2.9 \cdot 10^{-4}$  Jy beam $^{-1}$  at 1.5 GHz and  $4.4 \cdot 10^{-5}$  Jansky beam $^{-1}$  at 4.9 GHz. The northern lobe of 3C 219 has a rather irregular shape and no clear hot spot (Clarke et al. 1992). This leads to large ambiguities in the determination of its length or the geometrical parameters needed for the model presented here. I therefore only used the southern lobe which has a length of 40.4" and an aspect ratio at its widest point of  $R'_T = 1.6$ . The lobe is covered by 9.4 independent beams along the jet axis and by 5.9 beams perpendicular to it. The jet and counter-jet in 3C 219 are unusually bright and so the jet emission was removed from the maps of the southern lobe. For the 1-dimensional comparison method, I extracted  $S_\nu(l)$  along a line off-set by 2" to the south of the line connecting the core of the source with the hot spot of the southern lobe. This avoids con-

tamination of the surface brightness distribution by the jet emission. The hot spot in the southern lobe of 3C 219 is somewhat set back from the edge of the lobe. An aperture with a radius of  $4.3''$ , i.e. the width of the telescope beam, centered on the surface brightness peak was removed from the maps. For the 1-dimensional comparison, only values of  $S_\nu(l)$  core-wards of the hot spot were used.

The parameters of the best-fitting model are given in Table 3. The uncertainties of the model parameters is comparable to those found for the two lobes of Cygnus A. The angle to the LOS of 3C 219 is found to be smaller than that of Cygnus A. Since 3C 219 is a broad line radio galaxy this is in the expected sense, but the value of  $\theta$  predicted by the model is about double that inferred from the flux ratio of the jet and counter-jet. As mentioned above, the jets of 3C 219 are unusually bright and this may reflect some enhanced disruption of the jet flow by turbulence or even a complete restart of the jets in this source (Clarke & Burns 1991). The latter possibility has let Schoenmakers et al. (2000) to include this source among their examples of Double-Double Radio Galaxies (DDRG). The morphology of these sources strongly suggests restarting jets (Kaiser et al. 2000). The large jet to counter-jet flux ratio of 3C 219 may therefore be caused by effects other than relativistic beaming. The best-fitting value of  $\theta = 65^\circ$  is consistent with orientation-based unification schemes.

The central density of the gas surrounding 3C 219,  $\rho_o$ , predicted by the model is considerably smaller than that inferred from X-ray observations. To derive  $\rho_o$  I used  $a_o = 141$  kpc (Hardcastle & Worrall 1999). This discrepancy will be discussed in Sect. 6.

### 5.3. 3C 215

This source is a radio-loud quasar at  $z = 0.411$  with very irregular morphology (Bridle et al. 1994). I obtained raw observational data from the VLA archive at 1.5 GHz in A-array and 4.9 GHz in B-array. The 1.5 GHz observations were carried out by Miley in May 1986 while the 4.9 GHz observations were taken by Hough in December 1987. Again standard reduction with AIPS was performed on the data and resulted in two maps with an angular resolution of  $1.9''$ . The maps were restored using a pixel size of  $0.3'' \times 0.3''$  and the rms noise is  $1.6 \cdot 10^{-4}$  Jansky beam $^{-1}$  at 1.5 GHz and  $4.0 \cdot 10^{-5}$  Jansky beam $^{-1}$  at 4.9 GHz. The southern half of 3C 215 is very distorted with the jet bending in various places with enhanced surface brightness (Bridle et al. 1994). This part of the source is not consistent with a regular FR II-type lobe morphology and resembles in its outer regions an FR I-type structure. Therefore no attempt was made to apply the model to the southern part of the source. The northern lobe is more regular, however, the hot spot here is weak and the lobe widens considerably close to the core in a north-eastern direction. The lobe has a length of  $26.6''$  and its aspect ratio  $R'_T$  at the point where the width of the lobe is great-

est is 1.2. The hot spot in the northern lobe is not located at the very edge of the lobe similar to the southern lobe of 3C 219. An aperture centered on the surface brightness peak with a radius  $3.8''$  corresponding to the size of two telescope beams was removed from the map. For the 1-dimensional comparison the surface brightness distribution was extracted along a line off-set by about  $2''$  to the east from the core-hot spot direction to avoid emission from the jet. Again only pixels core-wards from the hot spot were used in the 1-dimensional case. The northern lobe of 3C 215 is covered by 14.0 independent beams along the jet and 11.7 beams at the widest point perpendicular to the jet.

Parameters of the best-fitting model and the derived properties of the environment of 3C 215 are given in Tables 3 and 4. The uncertainties for the model parameters are considerably larger for this source than for the two previous ones. The viewing angle to the jet axis,  $\theta$ , is smaller than for Cygnus A or 3C 219. This is again consistent with the predictions of unification schemes as 3C 215 is a quasar. The smaller observed value is again inferred from the flux ratio of the jet and counter-jet of 3C 215 (Bridle et al. 1994). Similarly to 3C 219 this ratio may be increased in 3C 215 because of the distorted morphology of its large scale radio structure. The southern jet does not seem to be embedded in a cocoon and it is therefore unlikely that the two jets are intrinsically identical. The flux ratio probably reflects physical processes other than purely relativistic beaming.

For the determination of  $\rho_o$  I used  $a_o = 204$  kpc from Hardcastle & Worrall (1999). The density of the gaseous environment of 3C 215 is predicted to be much lower than inferred from X-ray observations. Discussion of this point is deferred to Sect. 6.

## 6. Discussion

### 6.1. 1-D versus 2-D method

In general it is expected that an increase in the amount of information available to a given model fitting procedure should decrease the uncertainty in the determination of the model parameters. Comparing the results of the 1 and 2-dimensional methods for the lobes of Cygnus A one would therefore expect that the parameter uncertainties decrease for the higher resolution maps. This is indeed the case for the 2-dimensional method, particularly for the western lobe. However, the 1-dimensional method shows the opposite. Here the uncertainties are larger for the higher resolution maps. This is caused by the attempt to fit a very smooth model for the surface brightness to observational data which shows considerably greater local variations than the model. The fact that the model is unable to fit the local surface brightness structure observed was already noted in the previous Sect.. In the 2-dimensional case the off-axis parts of the cocoons provide

additional information and the influence of local structure is therefore to some extent averaged out in the fitting procedure. In other words, the 2-dimensional method is able to make use of the larger amount of information in higher resolution maps. The 1-dimensional method is restricted to a cut through the lobe. Here, the averaging effect of a larger telescope beam provides for a smoother surface density profile and the model fits the data better.

In the case of radio maps of low resolution which do not or only barely resolve the lobes perpendicular to the jets along most of their lengths, the 2-dimensional maps add little information to 1-dimensional cuts along the lobes. In these cases the additional model parameter  $p$  in the 2-dimensional method presented here allows the model to fit the data with a large range of parameter combinations. The uncertainties of the model parameters are then larger than for the 1-dimensional method. This effect can be seen for 3C 215 and, to a lesser extent, for the low resolution maps of the western lobe of Cygnus A. It is of course possible to fix the value of  $p$  for the 2-dimensional method as well but this does not significantly improve the constraints on the model parameters compared to the 1-dimensional method.

Which method is the best to use for a particular set of radio maps depends on the quality of the maps. If the radio lobes are well resolved along to the jet axis as well as perpendicular to it then the 2-dimensional methods will provide better constraints. However, it is computationally expensive. In the case of poorer resolution the 2-dimensional method will not add anything to the results obtained from a 1-dimensional comparison. For heavily distorted lobe structures both methods will fail but the 1-dimensional method may still provide order of magnitude estimates if the lobes are not entirely dominated by bright localised structure.

### 6.2. Determination of viewing angles

Orientation-based unification schemes attempt to explain radio galaxies and radio-loud quasars as essentially the same type of objects albeit viewed at different angles to the jet axis (Barthel 1989). The broad line radio galaxies may then be identified as the low redshift analoga to radio-loud quasars. These unification schemes imply that the viewing angle,  $\theta$ , to the jet axis is greater than about  $45^\circ$  for radio galaxies and smaller for quasars. Tests of this hypothesis are often inconclusive as the determination of  $\theta$  is difficult in practice.

As described above, the viewing angle  $\theta$  may be determined from radio observations alone. However, since the model depends mostly on  $\sin\theta$ , the uncertainties are large particularly for  $\theta \geq 45^\circ$ . Fortunately, the other model parameters and the source and environment properties inferred from these do not depend strongly on  $\theta$  and its error in this range. This agrees with the results of Wan & Daly (1998) who study the effects of the viewing angle on

the determination of a variety of source properties in great detail. The source orientation can only be determined accurately if the 2-dimensional comparison method is used on radio maps well resolved perpendicular to the jet axis. This agrees with the findings of Wan & Daly (1998) who use a different source model. Despite the large uncertainties in the model results presented here it is interesting to note that for the three sources studied the best-fitting values of  $\theta$  are smaller for the quasar (3C 215) and the broad line radio galaxy (3C 219) than for the radio galaxy (Cygnus A).

### 6.3. Environments of FR II sources

As I showed above, the model parameters of the best-fitting models can be used to infer the density parameter,  $\rho_o a_o^\beta$ , describing the density distribution in the environment of FR II objects. It is impossible using just this model to separate this into the central density,  $\rho_o$ , and the core radius,  $a_o$ . Furthermore, the model is insensitive to the slope,  $\beta$ , of the external density profile (see Sect. 4.3). To infer central densities, values for the core radius and  $\beta$  must be taken from other observations. In Table 4  $\rho_o$  for the three example sources is shown for the core radii given by Hardcastle & Worrall (1999) and  $\beta = 1.5$ . As noted in Sect. 5, the central densities found for 3C 219 and 3C 215 are inconsistent with those derived from the X-ray observations.

In several studies it was found that the pressure of the FR II source environment derived from X-ray observations apparently exceeds the pressure inside the radio lobes (e.g. Hardcastle & Worrall 2000 and references therein). The discrepancy in density found here is essentially the same phenomenon in the framework of isothermal density distributions for the source environments as described by the  $\beta$ -model, Eq. (1). All recent models for the evolution FR II sources, including the one discussed here, are based on the assumption that the cocoon is overpressured with respect to its surroundings. The X-ray observations seem to contradict this assumption.

Can the discrepancies be resolved? In the model described here I approximate the density distribution in the source environment, assumed to follow the  $\beta$ -model, by power laws. For cocoons extending well beyond the core radius the exponent of the power law is given by  $\beta = 3\beta'$ . In the case of Cygnus A this is justified as both lobes extend over more than 100 kpc while  $a_o = 24$  kpc. In the analysis  $\beta = 1.5$  was used which is identical with the result of Hardcastle,  $\beta' = 0.5$ . For 3C 219 and 3C 215  $\beta' = 0.9$  from the X-ray observations and in both sources the radio lobes only extend to about  $1.3a_o$ . Formally the model cannot be applied to these two sources because the underlying dynamical model is valid only for  $\beta \leq 2$  or  $\beta' \leq 2/3$ . However, as the cocoons in both sources do not extend much beyond the core radius, the density distribution in the environments of 3C 219 and 3C 215 are well repre-



sented by a power law with exponent  $\beta = 1.5$ . In these cases  $\rho_o$  found from the model is not identical to the central density of the  $\beta$ -model. From Eq. (1) it can be seen that the latter is given by  $\rho_o (1 + x^2)^{3\beta'/2} = 3.8\rho_o$ , where  $x$  is the length of the radio lobe in units of  $a_o$ . This correction is insufficient to make the model results consistent with the X-ray observations of 3C 219 and 3C 215.

X-ray observations of the hot gaseous environment of AGN are influenced by the presence of the active galaxy. Before the environment properties can be extracted, the bright X-ray emission of the AGN itself appearing as a point source must be carefully removed. In the case of radio-loud objects the large scale structure caused by the jets can also alter the X-ray emission of its surroundings. The magnitude of these effects is difficult to estimate if the X-ray observations do not fully resolve the scale of the cocoon. The hot spots at the end of the jets are strong sources of inverse Compton scattered X-ray photons. When resolved, these inverse Compton scattered photons are found to distort the X-ray contours of the extended emission (Cygnus A, Carilli et al. 1994; 3C 295, Harris et al. 2000). The more extended cocoon material itself may also act as a scatterer of CMB photons or of AGN emission (Brunetti et al. 1999). Finally, the bow shock surrounding the cocoon compresses and heats the gas in the source environment. Kaiser & Alexander (1999b) give an estimate for the expected X-ray luminosity from this shocked layer of gas,

$$L_x \sim 9.1 \cdot 10^{13} \frac{I^2}{a_2} \frac{(\rho_o a_o^\beta)^2}{a_1} L_j^{(7-5\beta)/3} \sqrt{P/R} \\ \times \left[ \exp\left(-4.0 \cdot 10^{-7} a_1^2 L_j^{(4-2\beta)/3} \nu/P/R\right) \right]_{\nu_2}^{\nu_1}, \quad (21)$$

where two typographical errors are corrected. Expressions for  $I^2/a_2$ ,  $a_1$  and  $P/R$  may be found in Kaiser & Alexander (1999b). The square brackets mean the difference of the exponential function at the limits of the observing band  $\nu_1$  and  $\nu_2$  in the rest frame of the source. The resulting X-ray luminosity can be converted to a ROSAT count rate using the internet version of PIMMS<sup>1</sup>. For the best-fitting model parameters for Cygnus A this implies that roughly 2% of all counts of the ROSAT observations presented by Hardcastle & Worrall (2000) attributed to the entire extended emission come from the layer of shocked gas in between bow shock and cocoon of this source. For 3C 219 this region around the southern lobe alone contributes about 10% of the relevant counts. The contribution of the northern lobe of 3C 215 is negligible ( $\sim 0.1\%$ ). However, in this case at least three very compact radio emission regions along the distorted jets are detected which may be powerful inverse Compton sources

(Bridle et al. 1994). Only X-ray observations resolving the scale of the radio structure in this and other sources will allow us to determine the contribution to the total X-ray emission from such compact regions and hot spots.

Even without detailed observations it is clear that powerful radio sources can contribute significantly to the extended X-ray emission in the central part of their environments. Helsdon & Ponman (2000) show for the case of loose groups of galaxies that such an overestimate at the centre of an X-ray surface brightness profile may lead to overestimates of the core radius and also of  $\beta'$  when fitted with a  $\beta$ -model. Using these overestimated values of  $a_o$  and  $\beta$  then yields values for  $\rho_o$  which are too low compared to the ‘real’ central density. An exact analysis of the magnitude of this effect is beyond the scope of this paper. In any case, this effect may explain the discrepancies found between the two methods of estimating the central densities and pressures of the FR II environments.

## 7. Conclusions

In this paper an analytical model for the surface brightness distribution of the cocoons of FR II-type radio sources is developed. The model is based on the self-similar model of Kaiser & Alexander (1997, KA) and its extension by Kaiser et al. (1997, KDA). The cocoon is split into small volume elements, the temporal evolution of which is traced individually. These elements are then identified with cylindrical slices which are rotationally symmetric about the jet axis. The bulk backflow of these slices is determined self-consistently from the constraints on the cocoon shape. Thus a 3-dimensional model of the synchrotron emissivity is constructed. Projecting this along the LOS, the model yields surface brightness profiles in one or two dimensions in dependence of several model parameters. It is shown that a number of degeneracies prevent constraints to be placed on all parameters. Comparatively robust estimates can be found for the cocoon pressure,  $p_c$ , the source age,  $t$ , the angle of the jet to the LOS,  $\theta$ , and, if the 2-dimensional comparison method is used, the initial slope of the energy distribution of the relativistic particles,  $p$ .

The model may be viewed as an extension of the classical spectral aging methods. However, it accurately takes into account the loss history of the relativistic particles and the evolution of the magnetic field in the cocoon. The age estimates derived from the model are therefore accurate and not only lower limits. It is also shown that diffusion of relativistic particles cannot significantly distort the energy spectrum of the relativistic particles in the cocoon.

In Sect. 5 the model predictions were compared with observational data for the three sources Cygnus A, 3C 219 and 3C 215. The four free model parameters are constrained to within at least a factor 2. The uncertainties of the cocoon pressure are remarkably small, less than 50%, while the source ages are constrained by the model to within 80% or better. The errors on the viewing angle are

<sup>1</sup> PIMMS was programmed by K. Mukai at the High Energy Astrophysics Science Archive Research Center of NASA, available at <http://heasarc.gsfc.nasa.gov/Tools/w3pimms.html>

large as the model mainly depends on  $\sin\theta$  which changes in the range of orientation angles found here ( $31^\circ$  to  $90^\circ$ ) by only 52%. The uncertainties in the model parameters translate to errors in the determination of the jet power,  $Q_o$ , and the density parameter,  $\rho_o a_o^\beta$ . However, the resulting uncertainties still allow at least order of magnitude estimates for these quantities.

The model results do not depend strongly on the resolution of the radio observations used in the fitting procedure. The results for both lobes of Cygnus A derived at 1.3" and 5" resolution are consistent with each other within the errors. However, the uncertainties in the parameter determination increase significantly with decreasing resolution. For radio maps which barely resolve the lobes perpendicular to the jet axis, the 2-dimensional method adds little in terms of constraints on model parameters to the 1-dimensional method. From the examples studied here it is not possible to give a firm lower limit for the resolution of maps used to fit with the model. However, the parameter uncertainties calculated here suggest that at least 4 independent beams along the jet axis are required. As was pointed out in Sect. 3.4, distorted lobe structures may indicate large turbulent flows within the cocoon. As the model is based on the assumption of largely non-turbulent backflow it cannot be used for such irregular sources.

The model can be used to infer the viewing angle of FR II-type sources to the LOS. Despite the large uncertainties in this determination, the three sources modeled here show the dependence of  $\theta$  on the spectral type of the host galaxies expected from orientation-based unification schemes.

The central density of the source environments found using this model is consistent with X-ray observations in the case of Cygnus A. In the case of 3C 219 and 3C 215 the estimates are too low. These discrepancies may stem from overestimates from X-ray observations of the core radius,  $a_o$ , and slope,  $\beta$ , of the density distributions. They are caused by the contribution of the large scale structure, i.e. cocoons and hot spots, of the radio sources to the X-ray emission. The, at present, insufficient spatial resolution of X-ray maps prevents the removal of these contributions before the determination of  $a_o$  and  $\beta$ .

The model allows the simultaneous determination of a number of key parameters of extragalactic radio sources of type FR II. Together with the 1 and 2-dimensional comparison methods, it is straightforward to analyse large numbers of objects drawn from complete samples of extragalactic radio sources. The quality of the radio data needed is only moderate and will already be available for many of the objects in question. However, the large scale structure of the objects should be reasonably regular in the sense that large scale turbulent motion within the cocoon is unlikely. Within these limits the method can provide order of magnitude estimates for the properties of the sources and their environments. This may help to answer

some of the questions related to the cosmological evolution of the FR II population and unification schemes of radio-loud AGN.

### Acknowledgments

It is a pleasure to thank P. N. Best, J. Dennett-Thorpe, H. J. Hardcastle and M. Lacy for valuable discussions. I would also like to thank P. N. Best and A. P. Schoenmakers for help with the reduction of the radio data and J. Dennett-Thorpe for providing the maps of 3C 219. Many thanks to the anonymous referee for valuable comments.

### References

- Alexander P., Leahy J.P., 1987, MNRAS 225, 1  
 Arshakian T.G., Longair M.S., 2000, MNRAS 311, 846  
 Barthel P.D., 1989, ApJ 336, 606  
 Begelman M.C., Cioffi D.F., 1989, ApJ 345, L21  
 Birkinshaw M., Worrall D.M., 1993, ApJ 412, 568  
 Black A.R.S., 1992, *Jets, wings and hotspots - The complex nature of powerful radio galaxies*, Ph.D. thesis, University of Cambridge  
 Blundell K.M., Rawlings S., 1999, Nat 399, 330  
 Blundell K.M., Rawlings S., 2000, AJ 119, 1111  
 Blundell K.M., Rawlings S., Willott C.J., 1999, AJ 117, 677  
 Blundell K.M., Rawlings S., Willott C.J., Kassim N.E., Perley R.A., 2000a, in J. Biretta and J. P. Leahy (eds.), *Lifecycles of Radio Galaxies*. New Astronomy Reviews, astro-ph/9910158  
 Blundell K.M., Kassim N.E., Perley R.A., 2000b, in R. D. Ekers et al. (ed.), *The universe at low radio frequencies*. ASP Conference Series, astro-ph/0004005  
 Bridle A.H., Hough D.H., Lonsdale C.J., Burns J.O., Laing R.A., 1994, AJ 108, 766  
 Brunetti G., Comastri A., Setti G., Feretti L., 1999, A&A 342, 57  
 Carilli C.L., Perley R.A., Dreher J.W., Leahy J.P., 1991, ApJ 383, 554  
 Carilli C.L., Perley R.A., Harris D.E., 1994, MNRAS 270, 173  
 Chuvilgin L.G., Ptuskin V.S., 1993, A&A 279, 278  
 Chyży K.T., 1997, MNRAS 289, 355  
 Clarke D.A., Burns J.O., 1991, ApJ 369, 308  
 Clarke D.A., Bridle A.H., Burns J.O., Perley R.A., Norman M.L., 1992, AJ 385, 173  
 Crawford C.S., Lehmann I., Fabian A.C., Bremer M.N., Hasinger G., 1999, MNRAS 308, 1159  
 Dały R.A., 1994, ApJ 426, 38  
 Duffy P., Kirk J.G., Gallant Y.A., Dendy R.O., 1995, A&A 302, L21  
 Falle S.A.E.G., 1991, MNRAS 250, 581  
 Falle S.A.E.G., 1994, MNRAS 269, 607  
 Fanaroff B.L., Riley J.M., 1974, MNRAS 167, 31  
 Garrington S.T., Leahy J.P., Conway R.G., Laing R.A., 1988, Nat 331, 147  
 Hardcastle M.J., Worrall D.M., 1999, MNRAS 309, 969  
 Hardcastle M.J., Worrall D.M., 2000, MNRAS: submitted.  
 Hardcastle M.J., Alexander P., Pooley G.G., Riley J.M., 1999, MNRAS 304, 135  
 Harris D.E., Nulsen P.E.J., Ponman T.J. et al., 2000, ApJ 530, L81

- Helsdon S.F., Ponman T.J., 2000, MNRAS: submitted, astro-ph/0002051
- Hill G.J., Lilly S.J., 1991, ApJ 367, 1
- Hughes P.A., Miller L., 1991, in P. A. Hughes (ed.), *Beams and jets in astrophysics*. Cambridge University Press, p. 52
- Kaiser C.R., 2000, in J. Biretta and J. P. Leahy (eds.), *Lifecycles of Radio Galaxies*. New Astronomy Reviews, astro-ph/9908261
- Kaiser C.R., Alexander P., 1997, MNRAS 286, 215, [KA]
- Kaiser C.R., Alexander P., 1999a, MNRAS 302, 515
- Kaiser C.R., Alexander P., 1999b, MNRAS 305, 707
- Kaiser C.R., Dennett-Thorpe J., Alexander P., 1997, MNRAS 292, 723, [KDA]
- Kaiser C.R., Schoenmakers A.P., Röttgering H.J.A., 2000, MNRAS 315, 381
- Katz-Stone D.M., Rudnick L., 1994, ApJ 426, 116
- Katz-Stone D.M., Rudnick L., Anderson M.C., 1993, ApJ 407, 549
- Laing R.A., 1980, MNRAS 193, 439
- Laing R.A., 1988, Nat 331, 149
- Leahy J.P., Williams A.G., 1984, MNRAS 210, 929
- Leahy J.P., Muxlow T.W.B., Stephens P.W., 1989, MNRAS 239, 401
- Miley G., 1980, ARA&A 18, 165
- Muxlow T.W.B., Garrington S.T., 1991, in P. A. Hughes (ed.), *Beams and jets in astrophysics*. Cambridge University Press, p. 52
- Nath B.B., 1995, MNRAS 274, 208
- Neeser M.J., Eales S.A., Duncan-Green J., Leahy J.P., Rawlings S., 1995, ApJ 451, 76
- Norman M.L., Smarr L., Winkler K.H.A., Smith M.D., 1982, A&A 113, 285
- Press W.H., Teukolsky S.A., Vetterling W.T., Flannery B.P., 1992, *Numerical Recipes. Second edition.*, Cambridge University Press, Cambridge, UK.
- Rechester A.B., Rosenbluth M.N., 1978, Phys. Rev. Lett. 40, 38
- Roland J., Hanisch R.J., Pelletier G., 1990, A&A 231, 327
- Rudnick L., Katz-Stone D.M., Anderson M.C., 1994, ApJ Supp. 90, 955
- Sambruna R.M., Eracleous M., Mushotzky R.F., 1999, ApJ 526, 60
- Sarazin C.L., 1988, *X-ray emission from clusters of galaxies*, Cambridge University Press, Cambridge.
- Scheuer P.A.G., 1974, MNRAS 166, 513
- Scheuer P.A.G., 1982, in D. S. Heeschen and C. M. Wade (eds.), *Extragalactic radio sources*. Reidel, p. 163
- Scheuer P.A.G., 1995, MNRAS 277, 331
- Schoenmakers A.P., de Bruyn A.G., Röttgering H.J.A., van der Laan H., Kaiser C.R., 2000, MNRAS 315, 371
- Shu F.H., 1991, *The physics of astrophysics. Vol.1: Radiation*, University Science Books, Mill Valley
- Wan L., Daly R.A., 1998, ApJ 499, 614

## Appendix A: Diffusion of relativistic particles in the cocoon

### A.1. Quasi-linear anomalous diffusion

In the model it will be assumed that the magnetic field within the cocoon is completely tangled on a scale  $r_t$  much

smaller than the size of the cocoon,  $L_j$ . In this case the relativistic electrons can diffuse quickly within ‘patches’ of coherent magnetic field of a size  $r_t$ . However, it is difficult for them to escape their patch as this would involve diffusion perpendicular to field lines. In the presence of turbulent motion within the plasma underlying the magnetic field, patches can be stretched out and in this case the diffusion of charged particles into an adjacent patch becomes more likely. Duffy et al. (1995) calculate how far a given electrons has to travel along a field line in its original patch before the patch becomes so stretched out that it can escape. Note here that this treatment is valid only in the quasi-linear regime for which the relative amplitude of irregularities of the magnetic field is much smaller than the ratio of the turbulent correlation lengths perpendicular and parallel to the local magnetic field. The efficiency of this diffusion then depends crucially on whether the electron is able to travel this distance ballistically or whether it must diffuse along the field line. The more efficient ballistic regime requires that

$$r_g > \sqrt{\kappa_{\perp} t_e}, \quad (\text{A.1})$$

where  $r_g$  is the gyro-radius of the particle in the field,  $\kappa_{\perp}$  is the diffusion coefficient perpendicular to the field and  $t_e$  is the time it takes the particle to escape the patch. For a relativistic electron moving at speed  $v$  and corresponding Lorentz factor  $\gamma$  following Chuvilgin & Ptuskin (1993)  $\kappa_{\perp} = \epsilon \kappa_B / (\epsilon + 1)$  with  $\kappa_B = \gamma v^2 m_e c / (3eB)$  the Bohm diffusion coefficient and  $\epsilon = \nu_{\text{col}} / \nu_g$ , where  $\nu_{\text{col}}$  is the rate of collision of the particle and  $\nu_g$  is its gyro-frequency. For the assumption of Blundell & Rawlings (2000) that the coherence length of the magnetic field is roughly 10 kpc in all directions, the inequality (A.1) yields  $\epsilon < 7 \cdot 10^{-12}$  for a magnetic field strength of 130  $\mu\text{G}$ , appropriate for the fiducial model of Sect. 4.3, and an electron with a Lorentz factor 1000. This implies that the time between collisions of this electron must be greater than 2 Myr, i.e. the mean free path of the electron is of order 600 kpc. This is clearly unphysical in the case of  $L_j \sim 100$  kpc as relativistic particles would then simply escape the cocoon very quickly.

The relativistic electrons in the cocoon must therefore diffuse along the magnetic field lines in between jumps from one patch of coherent magnetic field to another. The expression of Duffy et al. (1995) for the rms diffusion length after a time  $t$ ,  $x$ , in this case can be approximated by

$$x \sim \sqrt{-\frac{r_g c t}{3\epsilon \log(\sqrt{2\epsilon})}}. \quad (\text{A.2})$$

Assuming that the mean free path of the electron is less than the coherence length of the magnetic field, i.e. less than 10 kpc, I find for the same magnetic field and Lorentz factor  $x < 3$  kpc if  $t = 1$  Myr. A significant mixing of relativistic particles along the cocoon due to anomalous diffusion is therefore unlikely.

### A.2. Non-linear diffusion

Of course, it may be argued that as the above analysis only applies to the quasi-linear regime, the diffusion timescale in a highly turbulent flow may be much shorter. Consider such a flow to be present in the cocoons of FR II-type radio sources. In this case, the relativistic electrons may diffuse through the observed lobes within a time short compared to the age of the source. However, since diffusion is a stochastic process and the geometry of the cocoon is elongated, most of the particles will leave the cocoon sideways and will be lost to the surrounding gas before traveling large distances along the cocoon. It is likely that the diffusion time for the relativistic particles depends on their energy and so the diffusion losses, if present, will significantly change the emission spectrum which is not observed (e.g. Roland et al. 1990). Even in the case of efficient energy independent diffusion the observed radio lobes should show diffuse edges in low frequency radio maps. Again this is not observed (e.g. Roland et al. 1990, Blundell et al. 2000a,b).

From the above it is clear that in the presence of very efficient diffusion some special confinement mechanism for the relativistic particles in the cocoon preventing their escape sideways is needed. This may be provided for by the compression and shearing of the tangled magnetic field at the edges of the cocoon. This process will align the magnetic field close to the cocoon edge with this surface and therefore act as a kind of magnetic bottle. The order thus introduced in the originally tangled magnetic field due to this process leads to an enhanced polarisation of the emitted radiation in this region (e.g. Laing 1980).

Large volume compression ratios are ruled out as the sound speed in the cocoon is high (e.g. KA). However, for a conservative estimate consider a volume compression ratio of 10 in the sheet of compressed material at the edge of the cocoon of a given source. This already implies that the maximum theoretical value of polarisation of the synchrotron emission should be observed at the edge of the radio lobes (Hughes & Miller 1991). For adiabatic compression of a tangled magnetic field the strength of the field increases by a factor of roughly 4.6. The rate of collisions of a given particle is probably increased as well as the irregularities in the magnetic field are also compressed. However, the case of  $\nu_{\text{col}} = \text{const.}$  provides for a lower limit of  $\epsilon$  and so with  $\kappa_{\perp} = \epsilon\kappa_{\text{B}}/(\epsilon + 1)$  it is clear that the diffusion coefficient within the compressed region perpendicular to the field lines decreases by a factor 25 at most compared to the inner cocoon. This implies that in a given time a relativistic particle diffuses a 5 times shorter distance in the compressed boundary layer compared to the inner regions of the cocoon. To significantly influence the time the particle remains in the cocoon this compressed layer must at the very least occupy 20% of the width of the cocoon which is unlikely. Note, that although the magnetic field is compressed in the boundary

layer and therefore aligned with the cocoon surface some field lines may still be perpendicular to this surface. Along these field lines diffusion will be even faster allowing many electrons to escape the cocoon.

From this I conclude that diffusion, even if it is highly effective in the inner cocoon and there exists a compressed boundary layer along the edges of the cocoon, will not alter the distribution of relativistic particles within the cocoon. This allows us to use the spatial distribution of the synchrotron radio emission of FR II sources to infer their age. The model developed in the following can be viewed as an extension to the classical spectral aging methods in that it takes into account the evolution of the magnetic field in the lobe